EXPERIMENTS ON STRONGLY CORRELATED MATERIALS: MAGNETO-TRANSPORT PROPERTIES OF VO_2 AND V_2O_3

A THESIS SUBMITTED TO
THE GRADUATE SCHOOL OF ENGINEERING AND SCIENCE
OF BILKENT UNIVERSITY
IN PARTIAL FULFILLMENT OF THE REQUIREMENTS FOR
THE DEGREE OF
MASTER OF SCIENCE
IN
MATERIALS SCIENCE AND NANOTECHNOLOGY

By
Engin Can Sürmeli
September 2019

EXPERIMENTS ON STRONGLY CORRELATED MATERIALS: MAGNETO-TRANSPORT PROPERTIES OF VO_2 AND V_2O_3
By Engin Can Sürmeli
September 2019

We certify that we have read this thesis and that in our opinion it is fully adequate, in scope and in quality, as a thesis for the degree of Master of Science.

T. Serkan Kasırga(Advisor)

Engin Durgun

Talha Erdem

Approved for the Graduate School of Engineering and Science:

Ezhan Karaşan
Director of the Graduate School

ABSTRACT

EXPERIMENTS ON STRONGLY CORRELATED MATERIALS: MAGNETO-TRANSPORT PROPERTIES OF VO_2 AND V_2O_3

Engin Can Sürmeli
M.S. in Materials Science and Nanotechnology
Advisor: T. Serkan Kasırga
September 2019

Vanadium oxides provide unusual electrical and magnetic phenomena emerging from strong electronic correlations, which include, among other things, a thermally induced metal-insulator transition (MIT). Investigation of the changes in carrier concentration and mobility across the MIT in vanadium oxides, such as vanadium dioxide (VO_2) and vanadium sesquioxide (V_2O_3), carries great importance for understanding the micromechanisms behind such first-order phase transitions. A well-known approach to measuring such parameters in semiconductor materials is Hall effect measurement.

So far, magnetotransport studies have only been conducted on polycrystalline thin films of VO_2/V_2O_3. As a result, reports on the Hall mobility of these materials often contradict with each other due to the non-uniform stress building on the crystal by adhesion to the substrate. Thus, a thorough investigation of Hall effect measurements on single-crystalline, stress-free VO_2 nanobeams and V_2O_3 nanoplates is required. However, achieving this task is not a straightforward process. First of all, the relatively small size of nanobeams compared to the epitaxial films creates the necessity to utilize a bridge-type Hall-bar shaping of the crystal. Additionally, in order to produce a stress-free environment, the crystals must be detached from the substrate and transferred to an atomically flat surface, such as hexagonal boron nitride (h-BN). Therefore, the device fabrication method demands many steps despite that VO_2 is a very fragile material.

In this work, we provide a new fabrication method for shaping VO_2 and V_2O_3 into Hall-bar structure via Gallium and Argon-ion milling while inducing minimal damage on the crystal. We also investigate the strain level of shaped crystals and provide methods to prevent cracking in the devices upon structural phase

transition.

As a second objective, we investigate the resistivity behavior and magnetic response of VO_2 nanobeams at low temperature ranges. We show that the high magnetoresistance of VO_2 creates demand for very high magnetic fields in the Hall effect measurements.

Finally, we demonstrate a Hall effect measurement on an as-grown V_2O_3 nanoplatelet across its phase transition.

Keywords: vanadium dioxide, vanadium sesquioxide, strongly correlated materials, metal-insulator phase transition, Hall effect.

ÖZET

GÜÇLÜ ETKİLEŞİMLİ MALZEMELER ÜZERİNDE DENEYLER: VO_2 VE V_2O_3 KRİSTALLERİNİN MANYETO-TAŞIYICI ÖZELLİKLERİ

Engin Can Sürmeli
Malzeme Bilimi ve Nanoteknoloji, Yüksek Lisans
Tez Danışmanı: T. Serkan Kasırga
Eylül 2019

Vanadyum oksitler, diğer özelliklerinin yanı sıra, metal-yalıtkan geçişi (MYG) içeren güçlü elektronik etkileşimleri temel alan olağandışı elektriksel ve manyetik özellikler gösterirler. Vanadyum dioksit (VO_2) ve vanadyum seskioksit (V_2O_3) gibi vanadyum oksitlerde MYG boyunca taşıyıcı konsantrasyonundaki ve hareketliliğindeki değişimlerin araştırılması, bu birinci dereceden faz geçişlerinin arkasındaki mikro mekanizmaları anlamak için büyük önem taşımaktadır. Yarı iletken malzemelerde bu tür parametrelerin ölçülmesi için iyi bilinen bir yaklaşım Hall etkisi ölçümüdür.

Şimdiye kadar, manyeto taşıma çalışmaları sadece VO_2/V_2O_3 polikristal ince filmleri üzerinde yapılmıştır. Bu nedenle, bu malzemelerin Hall hareketliliği hakkındaki raporlar, çoğu zaman kristalin alttaşa yapışmasından kaynaklanan stres oluşumu nedeniyle birbiriyle çelişir. Bu yüzden tek-kristal, stresten bağımsız VO_2 ve V_2O_3 nanokristalleri üzerindeki Hall etkisi ölçümlerinin kapsamlı araştırılması gerekmektedir. Ancak bu görevin başarılması basit bir işlem değildir. İlk olarak, epitaksiyel filmlere kıyasla nispeten küçük boyuttaki nanokristallerin kullanılması, kristalin köprü-tipi Hall-çubuğu şeklini alması gerekliliğini yaratır. Ek olarak, stressiz bir ortam üretmek için kristaller alttaştan ayrılmış ve altıgen boron nitrat (h-BN) gibi atomik olarak düz bir yüzeye aktarılmış olmalıdır. Bununla beraber, cihaz imalat yöntemi birçok adım gerektirmesine rağmen VO_2 çok kırılgan bir malzemedir.

Bu çalışmada, kristallerde minimum düzeyde hasara neden olurken, Galyum ve Argon-iyon aşındırma yoluyla VO_2 ve V_2O_3'i Hall-çubuğu yapısına şekillendirmek için yeni bir üretim yöntemi sunuyoruz. Ayrıca, şekillendirilmiş kristallerin gerilim seviyelerini araştırıp yapısal faz geçişi sırasında cihazlardaki çatlamayı

önleme yöntemleri sunuyoruz.

İkinci bir hedef olarak, düşük sıcaklık seviyelerinde VO_2 nanokristallerin direnç davranışını ve manyetik özelliklerini araştırdık. VO_2'in yüksek manyeto direncinin, Hall etkisi ölçümlerinde çok yüksek manyetik alanlar gerektirdiğini gösterdik.

Son olarak, faz geçişi boyunca nanokristal olarak yetiştirilen V_2O_3 üzerinde Hall etkisi ölçümünü gösterdik.

Anahtar sözcükler: vanadyum dioksit, vanadyum seskioksit, güçlü etkileşimli malzemeler, metal-yalıtkan faz geçişi, Hall etkisi.

Acknowledgements

I have joined SCMLab during the second year of my undergraduate studies in Bilkent. Being one of the first students of Dr. Serkan Kasırga's lab, I have had chance to take a (infinitessimally small) part in the foundations of a science group and witnessed the progress it has made during all those years. I would like to thank Dr. Kasırga for his guidance and support in my academic studies whenever I needed.

I appreciate the help of Mustafa Fadlelmula, Mehdi Ramezani, Naveed Mehmood, Hamid Reza Rasouli and Övünç Karakurt for their contributions in my experiments, without them this work could not be complete. I also acknowledge all past and current members of the SCMLab that I could had the chance to share the good times with.

I would like to thank Dr. Seymur Jahangirov for his fruitful and motivational discussions. I will always appreciate his philosophical views about life in academia.

I would like to acknowledge the Scientific and Technological Research Council of Turkey (TÜBITAK) for supporting this work under the grant numbers 116M226, 214M109 and 115F070.

I express my gratitudes towards all my friends, especially Görkem Bozkurt, Enes Aybar, Koray Yavuz, Onur Çakıroğlu, Yetkin Pulcu, Özge Beğli, Efe Işılak, Didem Dede and İnci Güler. They made my time in Bilkent unforgettable and I have felt an immense amount of joy from their friendship.

I feel deeply indebted to my partner in science, Duygu Mutlu. We went through the hardest parts of grad school together and she was always there to cheer me up and motivate me to keep on fighting the challenges. I think I am incredibly lucky to have her in my life.

I have always felt the unconditional love, care and support from my grandmother Nigar and grandfather Naci Pekcan. No one else could have done better than they did in making me become who I am today. I also would like to thank my brother Deniz and the rest of my family members for all the joyful moments we had together.

I dedicate this thesis to the memory of Metin and Meral Sürmeli.

Contents

1 Introduction **1**

1.1 Hall Effect Theory 1

1.2 Hall Effect Measurement Techniques 4

1.3 Properties of Vanadium Dioxide 9

1.4 Properties of Vanadium Sesquioxide 12

1.5 Motivation 15

1.6 Outline 16

2 Methods **17**

2.1 Device Fabrication 17

2.1.1 Crystal Growth and Transfer 17

2.1.2 Argon and Gallium ion milling 19

2.1.3 E-beam lithography 22

2.1.4 Metal Contact Evaporation and Wire Bonding 26

2.2 Characterization 27

2.2.1 Atomic Force Microscopy 27

3 Results and Discussion **29**

3.1 Ion damage analysis in crystal shaping 29

3.2 Cracking crystals during heating 34

3.3 Occasions of Device Failure 38

3.4 VO_2 Measurements 39

3.5 V_2O_3 Measurements 42

4 Conclusions and Future Work **46**

A Copyright Permissions **53**

List of Figures

1.1 An illustration of a simple Hall effect measurement system. 3

1.2 Lamella-type van der Pauw structures. 4

1.3 Bridge-type Hall-bar structures. 7

1.4 An ideal Hall-bar sample with 3:1 aspect ratio. Here, a VO_2 nanobeam is shaped by Ga-ion milling with a Focused Ion Beam instrument. 9

1.5 The atomic structure of VO_2 showing rutile (R) in the metallic and monoclinic (M1) in the insulating phases. 10

1.6 Band diagram of the *3d* bands in VO_2 around the Fermi level. . . 10

1.7 Evolution of Hall mobility of VO_2 across the MIT. 12

1.8 The phase diagram of V_2O_3. 13

1.9 The change in Hall mobility in V_2O_3 between 300-800 K. 15

2.1 SEM micrograph showing the layered nature of the V_2O_3 nanoplatelet. 19

2.2 **a** Shaping the crystal into the bridge-type Hall-bar geometry via Ga-ion milling. The ions only etch a small portion on top of the crystal. **b** The crystal is thinned down from ∼100 nm to 10 nm via Ar-ion milling. **c** The crystal is treated with HCl or BOE solution to remove the amorphous layer left by Ar-ion milling. This step restores the electrical properties of the crystal to a pristine form [32]. Each scalebar represents 10 μm. 21

2.3 The live-view camera system for determining the coordinates of a crystal on the wafer. 22

2.4 The orientation indicators (squares) and alignment marks (crosses) are used to align the crystal with the desired contact pattern. . . 24

2.5 The design process starts with outlining the alignment marks as shown in step **b**. Then, the contact regions are designed for the device as shown in **c-d**. Scalebars represent 20 μm. 25

2.6 **a** VO_2 and **b** V_2O_3 Hall-bars with the contact regions developed for metal evaporation. 26

2.7 Au/Cr contacts deposited onto the devices from Figure 2.6 27

2.8 BOE treatment reduces the thickness sample by 7 nm in 5 seconds dip. A further 15 seconds of dipping does not change the thickness, thus the oxide layer is completely removed from the sample. Each scalebar represents 4 μm. 28

3.1 SRIM results showing the Ga-ion damage on the VO_2 crystal with increasing number of ions. The maximum depth of implanted ions converge to 20 nm from the surface of the crystal. 30

3.2 SRIM results showing the Ar-ion damage on the VO_2 crystal with increasing number of ions. The maximum depth of implanted ions converge to 5.2 nm from the surface of the crystal. 31

3.3 Evolution of the Ar-ion distribution in the VO_2 crystal. Majority of the ions are located at 1.7 nm from the surface of the crystal. . . 32

3.4 HR-TEM image of a cross-section of etched VO_2 nanobeams. 33

3.5 Resistance vs temperature cycle of pristine, milled and HCl treated VO_2. 34

3.6 Two cracks appear on a 160 nm thick Hall-bar shaped VO_2 crystal during the MIT as a result of the stress introduced by the structural phase transition. 35

3.7 A 174 nm thick VO_2 crystal shaped into Hall-bar geometry cracks during the MIT as a result of the stress introduced by the structural phase transition. 36

3.8 Successful insulator-to-metal transition of a Hall-bar shaped VO_2 crystal. The crystal is thinned down to 10 nm thickness and treated with HCl to remove the amorphous surface layer. The transition starts taking place near the expected temperature for free-standing crystals (338 K [14]). Each scalebar represents 10 µm. 37

3.9 Successful insulator-to-metal transition of a Hall-bar shaped VO_2 crystal. The crystal is thinned down to 10 nm thickness and treated with HCl to remove the amorphous surface layer. The transition starts taking place near the expected temperature for free-standing crystals (338 K [14]). Each scalebar represents 10 µm. 38

3.10 Exploded Hall-bar and 4-terminal devices during electrical measurements. Scalebars represent 20 μm. 39

3.11 Optical image of a 4-terminal VO_2 device used in magnetoresistance measurements. 40

3.12 Resistivity vs. temperature curve of the 119 nm thick VO_2 device. The device failed while it reached 255 K during the heating cycle. 41

3.13 The change in the resistance of the device with response to perpendicularly applied magnetic field. Device temperature is kept at 100 K. 42

3.14 Optical image of a 6-terminal V_2O_3 device used to investigate the magnetotransport properties. 43

3.15 Resistance vs. temperature of the V_2O_3 device. A transition from PI to AFI phase of the device is observed at 188 K. 44

3.16 The response of the Hall voltage (V_H) to perpendicularly applied magnetic field in PI and AFI phases of the device. 45

List of Tables

2.1 Thickness data of various PMMA coating recipes. The rotation speed is 3000 rpm and duration is 40 seconds for each step. Thickness data in bold represents the recipes used in this work. 27

Chapter 1

Introduction

Vanadium oxides provide unusual electrical and magnetic phenomena emerging from strong electronic correlations, which include, among other things, a metal-insulator transition (MIT). The MIT can be induced thermally at a critical temperature for vanadium oxides [1], and can also be activated via doping [2], strain [3] or photo-excitation [4]. The strong physical interactions between the d and f electrons via spin, charge, lattice and orbital degrees of freedom makes these materials exceptionally sensitive to external stimuli such as strain, temperature and doping. Investigation of the changes in carrier concentration and mobility across the MIT in vanadium oxides, such as vanadium dioxide (VO_2) and vanadium sesquioxide (V_2O_3), carries great importance for understanding the micromechanisms behind such first-order phase transitions. A well-known approach to measuring such parameters in semiconductor materials is Hall effect measurement.

1.1 Hall Effect Theory

The strength of a material in conducting (or resisting) a flow of electric current, namely the electrical conductivity (resistivity), is proportional to the amount and

velocity of charge carriers inside the material. The average number of charge carriers per unit volume of a material is defined as the carrier concentration, and denoted by n for electrons and p for holes. Similarly, carrier mobility is a measure of the movement of charge carriers inside the material under the influence of electric field. It is denoted by μ_n for electrons and μ_p for holes. The carrier mobility depends on parameters such as the impurity and defect concentration in the material and temperature. Mobility is a key factor in semiconductor device performance in two aspects. First, at low electric fields the carrier velocity is proportional to the mobility, therefore high mobility devices show a high frequency response, because carriers take less time to travel through the device. Secondly, higher mobility devices can carry more current to charge capacitances more rapidly [5]. The conductivity (σ) of a semiconductor can be represented as a combination of carrier concentration and mobility in the following form:

$$\sigma = 1/\rho = q(\mu_n n + \mu_p p) \tag{1.1}$$

where ρ is representing the resistivity of the material, and q is the elementary charge. Now, we will shift our attention towards experimentally determining the carrier concentration and mobility of a semiconductor with Hall effect measurement.

Consider a slab of a rectangularly shaped material with thickness t and width w, as depicted in Figure 1.1. Assume that electrons are the dominant type of carriers in the system ($n \gg p$). An electric current flows in the x-direction and a perpendicularly aligned magnetic field ($\overrightarrow{B}$) cuts through the sample in the z-direction. The Lorentzian force created by the magnetic field will push the electrons in the (-y)-direction. The drifting of charge carriers on one side of the sample creates a potential difference along the y-direction and this can be measured as the voltage difference between the two sides of the samples, namely the Hall voltage V_H. The sign of V_H would be positive (negative) for p-type (n-type) materials.

As charge carriers drift to the side of the sample, they will create an electric field ($\overrightarrow{\xi_y}$) along the y-direction, opposing the Lorentzian force. When a steady state is reached, the net force on the charge carriers in the y-direction will be

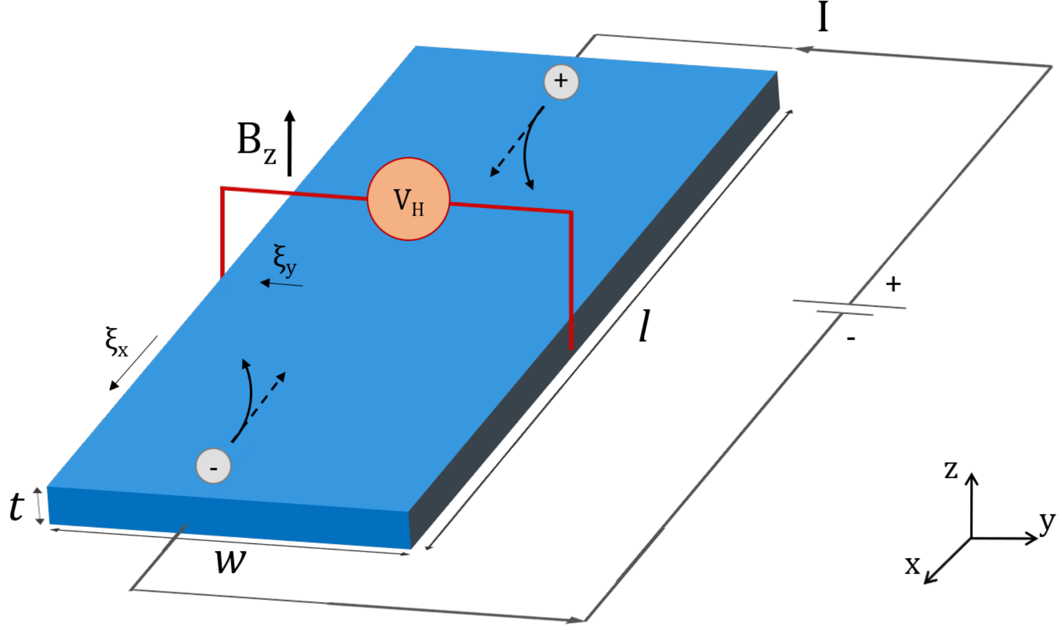

Figure 1.1: An illustration of a simple Hall effect measurement system.

zero. The Lorentz force acting on an electron can be written as $\overrightarrow{F_B} = -q(\overrightarrow{v} \times \overrightarrow{B})$ where $\overrightarrow{v}$ is the drift velocity. Similarly the Coulomb force acting on an electron is $\overrightarrow{F_E} = (-q)\overrightarrow{\xi_y}$. Therefore, the net force along the y-direction will be,

$$\overrightarrow{F_y} = -q(\overrightarrow{v} \times \overrightarrow{B}) + (-q)\overrightarrow{\xi_y} = 0$$

$$\Rightarrow qv_xB_z - q\xi_y = 0$$

$$\Rightarrow \xi_y = v_xB_z \tag{1.2}$$

$\overrightarrow{\xi_y}$ can be written in terms of the Hall voltage by the relation in Eq. 1.3. Also, we can express v_x in terms of electric current (I), electron concentration (n), charge, thickness and width of the material as follows:

$$\xi_y = \frac{V_H}{w}, \quad v_x = \frac{I}{-qntw} \tag{1.3}$$

Then substituting ξ_y and v_x in Eq. 1.2 with Eq. 1.3, and rearranging the terms would give the Hall coefficient R_H, which is defined as

$$R_H \equiv \frac{-1}{nq} = \frac{V_Ht}{IB_z} \tag{1.4}$$

Thus, one can calculate the carrier concentration (n) of a semiconductor as a function of the measurable parameters provided in Eq. (1.3) as

$$n = \frac{IB_z}{-qV_H t} \tag{1.5}$$

As we assumed the material to be n-type ($n \gg p$), the conductivity of the material from Eq. 1.1 can be written as $\sigma = nq\mu_e$. Combining this with Eq. 1.4, μ_H will become

$$\mu_H = \frac{\sigma}{nq} = \frac{|R_H|}{\rho} \tag{1.6}$$

1.2 Hall Effect Measurement Techniques

Hall effect measurements boil down to two device geometries, one being the van der Pauw (Figure 1.2) and the other the bridge-type Hall-bar (Figure 1.3) geometries. Both can be used to determine the carrier concentration and mobility of a semiconductor, though each of the methods have their own advantages and disadvantages.

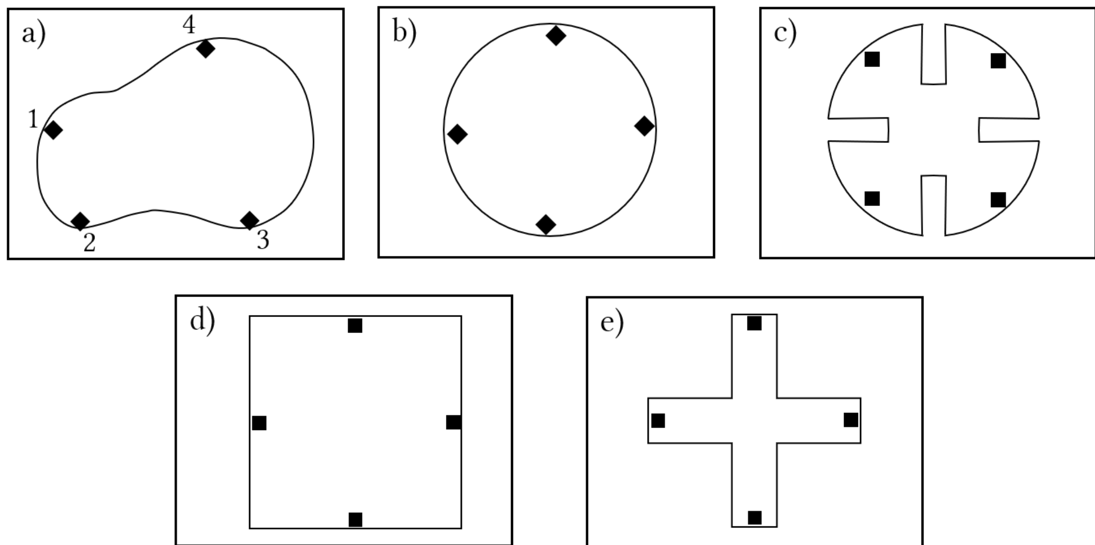

Figure 1.2: Lamella-type van der Pauw structures.

In 1958, van der Pauw [6] demonstrated how to measure the resistivity, carrier concentration and Hall mobility of a specimen of arbitrary shape as long as it fulfills the following requirements:

1. The sample is homogeneous in thickness.

2. The sample is singly connected, i.e. must not contain any isolated holes

3. The contacts are made sufficiently small and on located on the periphery of the specimen.

To find the resistivity of the specimen in Figure 1.2a, a current should be applied from the contacts 1 and 2, and the voltage generated between the contacts 3 and 4 should be measured. As a second step, current is applied from 2 and 3 and voltage is measured from 4 and 1. Then the resistivity of the sample of thickness t will be given by:

$$\rho = \frac{\pi t}{ln(2)} \frac{R_{12,34} + R_{23,41}}{2} F \tag{1.7}$$

where $R_{12,34} = V_{34}/I_{12}$ and similarly $R_{23,41} = V_{41}/I_{23}$. F is a function of $Q \equiv R_{12,34}/R_{23,41}$ that satisfies the following:

$$\frac{Q-1}{Q+1} = \frac{F}{ln(2)} arcosh\left(\frac{exp(ln(2)/F)}{2}\right) \tag{1.8}$$

For geometrically symmetric samples, $F = 1$. Otherwise, F is usually found with numerical methods.

Next, with a perpendicular magnetic field of $\overrightarrow{B}$ and a current through contacts 2 and 4 applied, and the Hall voltage between contacts 1 and 3 is measured. The Hall coefficient of the specimen is calculated by the following relation:

$$R_{H,C} = \frac{t}{B} \frac{V_{31}(+B) + V_{13}(-B)}{I_{42}(+B) + I_{24}(-B)} \tag{1.9}$$

To check for homogeneity of the sample, the same measurement should be done with exchanging the current and voltage contacts:

$$R_{H,D} = \frac{t}{B} \frac{V_{42}(+B) + V_{24}(-B)}{I_{31}(+B) + I_{13}(-B)} \tag{1.10}$$

If the values of $R_{H,C}$ and $R_{H,D}$ agree within $\pm 10\%$, then the average value of the Hall coefficient is:

$$R_{H_{av}} = \frac{R_{H,C} + R_{H,D}}{2} \tag{1.11}$$

From these two measurements, the carrier concentration and the mobility of the sample can be calculated with Eq. 1.5 and 1.6, respectively.

One disadvantage that this method brings is that, determination of the resistivity and Hall coefficient of a specimen with van der Pauw geometry requires two set of measurements to be done with different configurations. Thus, it takes about twice the time to make a Hall effect measurement in van der Pauw geometry compared to a device with Hall-bar geometry. A second type of disadvantage is, the amount of voltage required to pass a current from the contacts are determined by their size. Ideally the van der Pauw method should use point-like contacts that are made infinitesimally small in order to have minimal error in Hall effect measurements, but that would require a very high voltage level to be applied to the device, which would eventually result in failure. As the ratio of the width of the contact (c) to the width or length of the sample get larger, measurement error will increase. For example, if we consider the circular shape with diameter d in Figure 1.2b, with a ratio of $c/d = 1/6$, the measurement of the Hall coefficient will result in 13% error according to the report of American Society for Testing and Materials (ASTM) Standards F76 [7]. If the sample is shaped into a cloverleaf geometry (Figure 1.2c) the measurement error due to the contact size can be drastically decreased, as shown by van Daal [8], it reduces by a factor of 3-5 for the Hall coefficient. This structure is widely used in the literature for Hall effect measurements of semiconductor thin-films [9], [10], [11], [12], [13]. And in general, most thin-film devices are produced in van der Pauw geometry as they can support an achievable contact-to-body ratio owing to their large scale growth techniques. However, nanobeams and nanoplatelets, as the names suggest, can reach roughly 10 to 30 μm scale at maximum in terms of crystal body and therefore the contacts can not be made sufficiently small in a van der Pauw geometry. A better way to study Hall effect in nanobeams and nanoplatelets is through preparing bridge-type Hall-bar structures. In addition, Hall-bar structure is desirable for anisotropic semiconductors like VO_2 and V_2O_3

where the electrical properties depend on the direction of crystal axis.

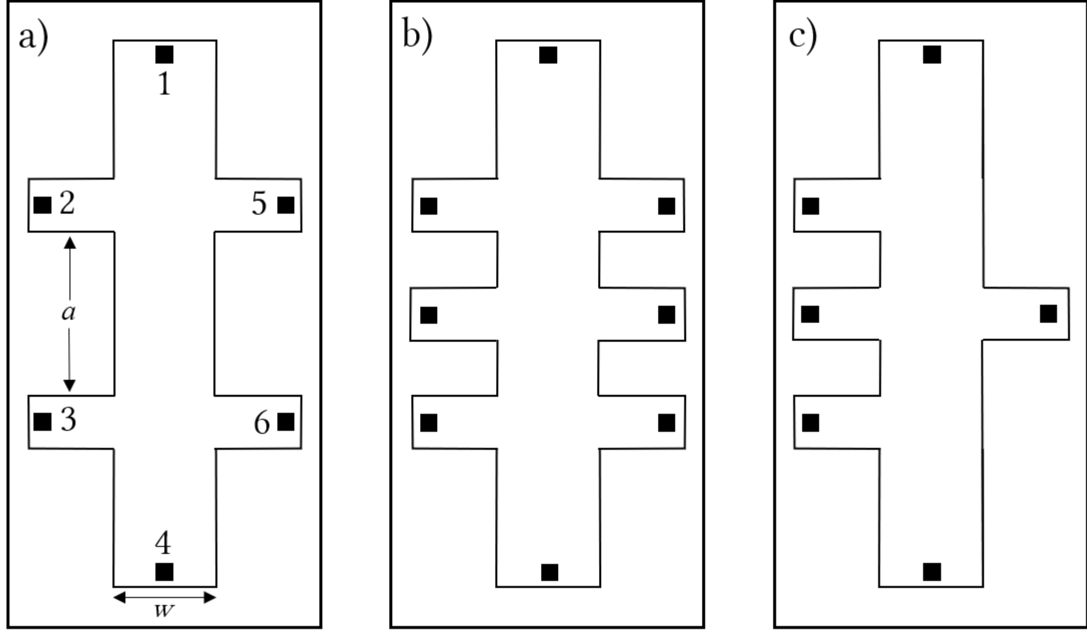

Figure 1.3: Bridge-type Hall-bar structures.

A Hall-bar device such as in Figure 1.3a, can be used to determine a semiconductor's carrier concentration and mobility as well. To begin with, the specimen must be shaped into the appropriate geometry via certain lithography methods such as ion or chemical etching. (see 'Argon and Gallium ion milling' - section 2.1.2). Similar to the van der Pauw method's requirements, the specimen should be uniform in thickness by $\pm 1\%$.

First, the resistivity of the specimen is determined with a 4-terminal measurement. Current is applied from contacts 1 and 4, and the voltage is measured from contacts 2 and 3. To check for homogeneity, the same measurement could be done from the opposite side contacts 5 and 6. With the device thickness of the sample being t, width w and distance between the side contacts a (indicated on Figure 1.3a), the resistivities will be given by:

$$\rho_A = \frac{wt}{a}\frac{V_{23}}{I_{14}}, \quad \rho_B = \frac{wt}{a}\frac{V_{56}}{I_{14}} \tag{1.12}$$

If the two measurements agree within $\pm 10\%$, the average resistivity of the sample

is:

$$\rho_{av} = \frac{\rho_A + \rho_B}{2} \tag{1.13}$$

Now without changing the configuration of the setup, the Hall coefficient can be measured under the influence of a magnetic field $\overrightarrow{B}$ that is perpendicular to the surface plane of the device. Once more, two set of measurements from the opposite side contacts is useful for checking the homogeneity of the sample. The Hall coefficient with the first set of side contacts is calculated with the following formula:

$$R_{H,A} = \frac{t}{B}\frac{V_{25}(+B) + V_{52}(-B)}{I_{14}(+B) + I_{41}(-B)} \tag{1.14}$$

And with the second set of side contacts:

$$R_{H,B} = \frac{t}{B}\frac{V_{36}(+B) + V_{63}(-B)}{I_{14}(+B) + I_{41}(-B)} \tag{1.15}$$

If the two values agree by $\pm 10\%$, the average value of the Hall coefficient of the sample will be:

$$R_{H,av} = \frac{R_{H,A} + R_{H,B}}{2} \tag{1.16}$$

From these two measurements, the carrier concentration and the mobility of the sample can be calculated with Eq. 1.5 and 1.6, respectively.

It is worth noting that, in a device with Hall-bar structure, the voltage reading between the side contacts might get shorted by the current flowing between the source and drain. This would put a significant influence on the measured Hall voltage and lead to inaccurate results. In order to avoid such issues, it is advised by ASTM Standard F76 that the length of the device should be 3 times longer than its width [7]. An SEM micrograph of an ideal Hall-bar sample with appropriate dimensions is provided in Figure 1.4.

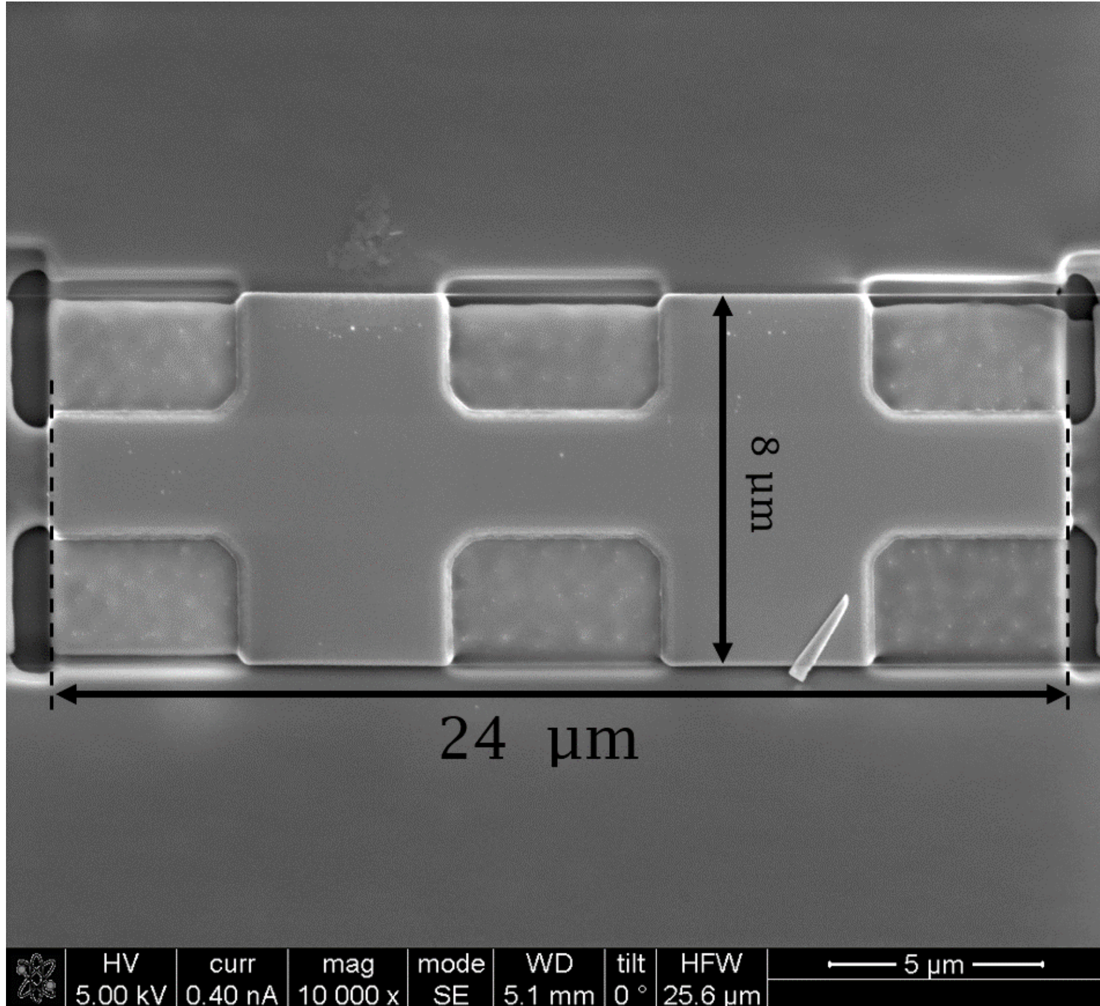

Figure 1.4: An ideal Hall-bar sample with 3:1 aspect ratio. Here, a VO_2 nanobeam is shaped by Ga-ion milling with a Focused Ion Beam instrument.

1.3 Properties of Vanadium Dioxide

VO_2 is a strongly correlated material which shows a metal-to-insulator transition that happens at a critical temperature $T_{c,VO_2} = 338$ K for free standing crystals [14]. Below T_c, VO_2 is a metal with rutile (R) tetragonal atomic structure, while it becomes an insulator with monoclinic M1 structure at elevated temperatures, which are illustrated in Figure 1.5. The conductivity of VO_2 increases by five

orders of magnitude across the MIT. Additionally, VO_2 crystals can be tensiley stressed to establish monoclinic M2 and triclinic (T) phases [15].

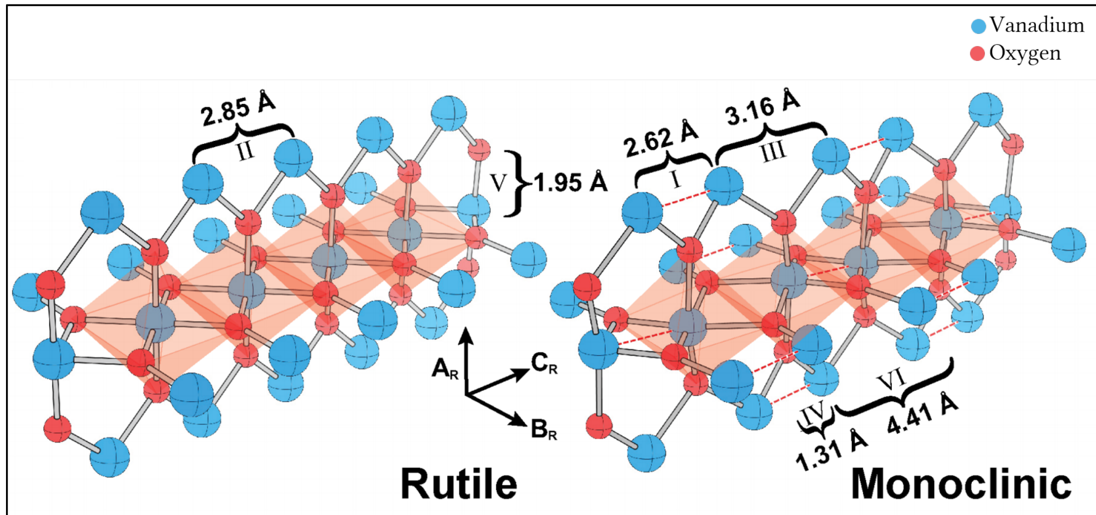

Figure 1.5: The atomic structure of VO_2 showing rutile (R) in the metallic and monoclinic M1 in the insulating phases. Taken from ref. [16].

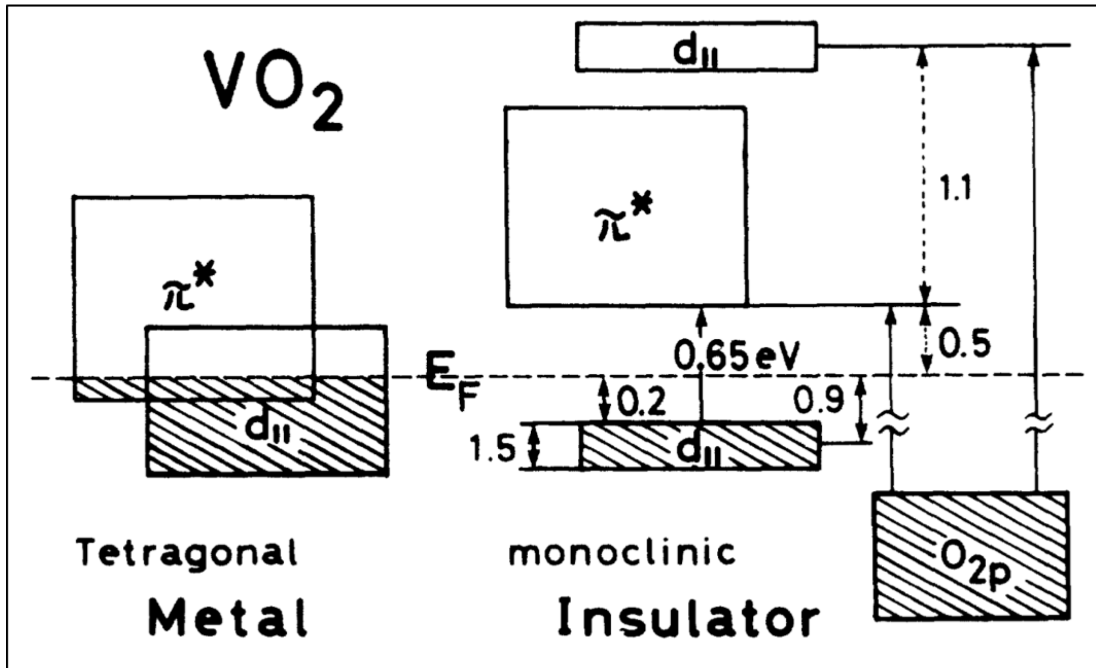

Figure 1.6: Band diagram of the *3d* bands in VO_2 around the Fermi level. Taken from ref. [17].

The band-gap of the insulating M1 phase is reported to be 0.7 eV [17], as shown in Figure 1.6, measured by the Ultraviolet Photoemission Spectroscopy technique. Several models have been proposed to explain the main mechanism behind the MIT in VO_2. A Peierls model based approach associates the structural phase transition happening at the critical temperature of vanadium oxides to a band-gap opening [18],[10]. In detail, the change in the periodic potential energy of the lattice affects the allowed energy states for the electrons, so that a new band gap occurs in the material. Another widely accepted approach is the Mott-Hubbard model, where the lattice potential energy is written as a function of the Thomas-Fermi screening constant which is defined in terms of the carrier concentration in the material. [18],[19]. The observed increase in the carrier concentration with increasing temperature reaches a critical point so that metallic state occurs in VO_2. Despite being studied over more than six decades [1], the nature of MIT still has not been understood properly due to complications arising from controlling external parameters like temperature, stress and doping.

According to Hall effect measurements performed on thin films of VO_2, the evolution of carrier concentration in VO_2 across the MIT increases by five orders of magnitude ($4\text{x}10^{18}$ per cm^{-3} in the insulating phase to $1.4\text{x}10^{23}$ per cm^{-3} in the metallic phase) [20],[21],[9]. However, the evolution of carrier mobility across the MIT is still under debate. To start with, *Rosevear et al.*'s [20] work claims that mobility drops as a function of the temperature T ($\mu_H \sim T^{-3/2}$) as the MIT happens. The drop in μ_H is about 40% (Figure 1.7a), and associated to the slowing of band electrons due to scattering from acoustic phonons of the material with increasing temperature. Next, *Ruzmetov et al.* [21] carried out the Hall measurements at magnetic fields up to 12 Tesla and found that the mobility was decreasing about 20% across the MIT (Figure 1.7b). More recently, *Yamin et al.* showed that mobility change is very insignificant (Figure 1.7c), therefore it cannot be attributed to the structural phase change happening during MIT. They have claimed that MIT is rather a macroscopic manifestation of the spatial phase separation of metallic and insulating regions in the crystal.

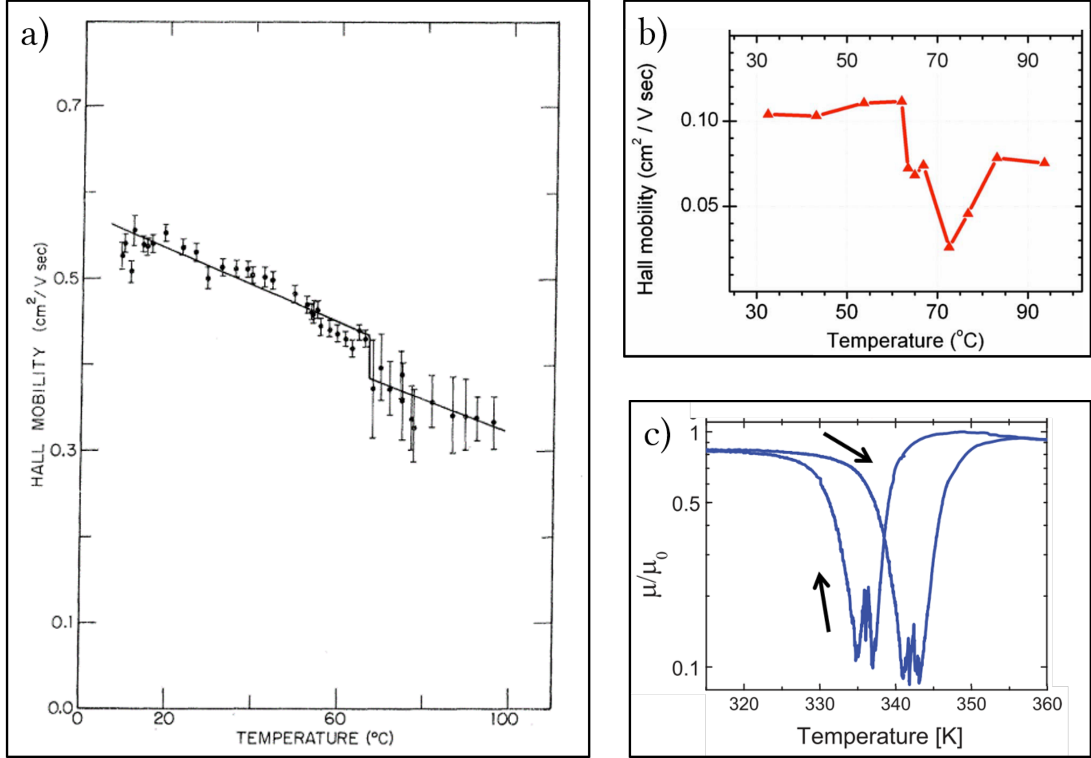

Figure 1.7: Evolution of Hall mobility of VO_2 across the MIT. Reproduced figures from ref. [20] (**a**), [21] (**b**), [9] (**c**).

1.4 Properties of Vanadium Sesquioxide

V_2O_3 is another member of the strongly correlated vanadium oxides family. As reported in the literature [22], V_2O_3 behaves as a paramagnetic metal (PM) or a paramagnetic insulator (PI) at room temperature, according to the compressive strain applied to the material. The material undergoes a structural phase transition below a critical temperature T_c ($T_c \approx 160$ K for free-standing crystals, where PM to AFI transition occurs), into the anti-ferromagnetic Mott insulator (AFI) state, though the transition temperature is highly dependent on external parameters such as strain and doping. The phase diagram of V_2O_3 as a function of compressive strain applied on the material is provided in Figure 1.8. For tensiley strained crystals above ∼400 K, the material enters a supercritical state

where the boundary between PI and PM phases disappear.

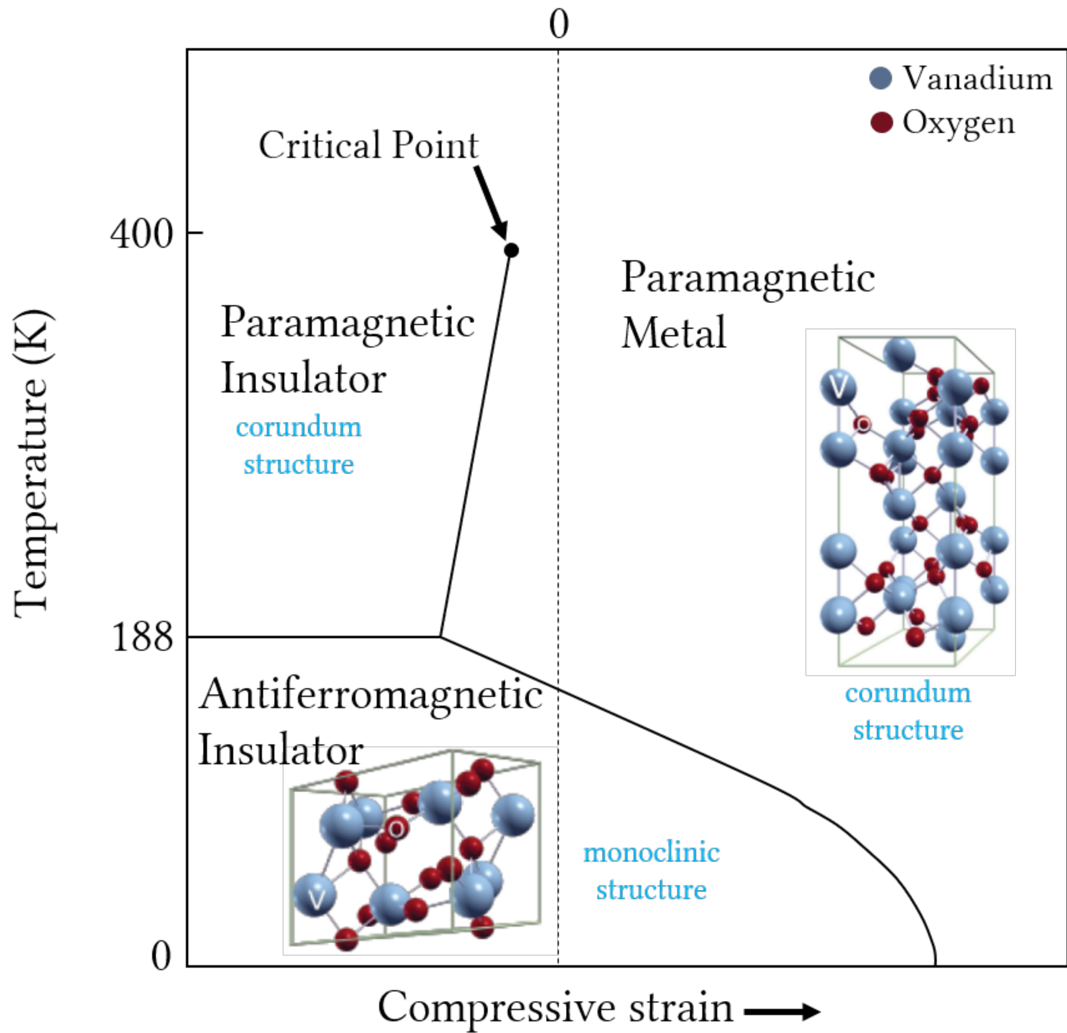

Figure 1.8: The phase diagram of V_2O_3 based on reference [22]. The paramagnetic metal (PM) and insulator (PI) phases have corundum structure, while the antiferromagnetic insulator phase (AFI) has a monoclinic structure.

Similar to VO_2, the exact nature behind the phase transition of V_2O_3 is still under debate. At the phase transition of V_2O_3, electronic, structural and magnetic transitions occur simultaneously. With so many degrees of freedom in effect at once, it is challenging to determine if either of them plays a dominant role for inducing the MIT. Aside from Peierls (structural) and Mott (electronic) models,

the Slater model attributes the opening of a band-gap to the change in the energy of the electrons with respect to the magnetic spin ordering inside the material [23]. A recent report by *Trastoy et al.* [24] claimed the origin of the phase transition (PM to AFI) in V_2O_3 to be the antiferromagnetic ordering of the insulating phase caused by the Coulomb interactions. They have observed that the magnetoresistance of the V_2O_3 began to change from positive to negative value instantly at the critical temperature where the phase transition is happening. Moreover, with considering a system with a single band Hubbard model at half filling and solving with dynamical mean-field theory, they could reproduce the magnetoresistance behavior of V_2O_3 at the MIT. In the light of these results they have concluded that the MIT in V_2O_3 comes from a Mott-Slater transition

Another study on the magneto-transport properties of V_2O_3 by *Austin et al.* have demonstrated that it is an n-type material in the metallic state near room temperature. Additionally, Hall measurements in the 300-800 K temperature range showed that carrier mobility changes from 0.6 to 0.2 $cm^2/V.s$ (Figure 1.9), and carrier concentration remains constant at 0.6 carriers per V atom throughout the this range [25]. It is worthy to note that this study is based on epitaxially grown V_2O_3, therefore the effect of strain due to lattice mismatch could not be eliminated. Recently, we have provided a method to reduce the strain on CVD grown V_2O_3 nanoplatelets by transferring on Si/SiO_2 substrate [26]. Furthermore, *Austin et al.*'s work only considers the high temperature regime where V_2O_3 is mostly in PM phase. We believe that a study of Hall measurements on free-standing V_2O_3 crystals could provide more accurate results on carrier concentration and mobility of the material across the insulating and metallic phases.

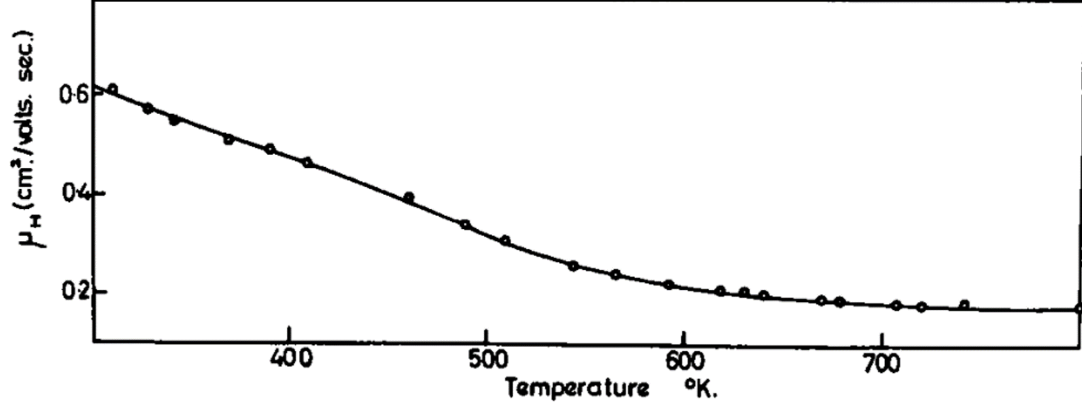

Figure 1.9: The change in Hall mobility in the PM phase of V_2O_3 between 300-800 K. Taken from ref. [25].

1.5 Motivation

With most of the studies concentrated on VO_2 polycrystalline thin films [10],[9],[27],[28] and thin or bulk single crystals [20],[29], the results on the Hall mobility of VO_2 often contradict with each other due to the non-uniform stress building on the crystal by adhesion to the substrate [30],[31]. Thus, a thorough investigation of Hall effect measurements on single-crystalline, stress-free VO_2 nanobeams is required. However, achieving this task is not a straightforward process. First of all, the relatively small size of nanobeams compared to the epitaxial films creates the necessity to utilize a bridge-type Hall-bar shaping of the crystal. Additionally, in order to produce a stress-free environment the crystals must be detached from the substrate and transferred to an atomically flat surface, such as hexagonal boron nitride (h-BN). Therefore the device fabrication method demands many steps despite that VO_2 is a very fragile material.

Similarly, studies on the Hall carrier concentration and mobility of V_2O_3 have been conducted on epitaxial thin films and they only report those parameters in high temperature regimes. A Hall effect measurement on the lower temperature AFI phase would also provide better understanding for the mechanisms behind the first-order phase transitions in V_2O_3.

Finally, it has been shown in a previous work of ours that when VO_2 nanobeams are milled in a controlled manner to achieve thickness even below 4 nm, the nanocrystals retain their pristine electrical properties [32]. Further milling of the crystals may bring them to a limit where the charge carriers inside the material feel a two-dimensional confinement. If such a limit is achieved, the behavior of carriers can be investigated with Hall effect measurements. The same investigation can be applied to V_2O_3 nanoplates in the monolayer limit as well.

1.6 Outline

The first part of the thesis is dedicated to device fabrication methods, where we explain how to shape VO_2/V_2O_3 crystals into Hall-bar structures with Gallium and Argon ion milling (Ion damage analysis is provided in the next chapter). We also provide optimal recipes for e-beam lithography process where we pattern the devices for metal contact evaporation.

The second part is dedicated to overcoming some of the challenges with Hall effect measurements brought by working on VO_2 nanobeams, such as cracking crystals upon phase transition and the need for a bridge-type Hall-bar shaping with minimal ion implantation. Furthermore, we investigate the resistivity behavior and magnetic response of a VO_2 nanobeam between 120-300 K.

In the third part of the thesis we demonstrate a Hall effect measurement of an as-grown V_2O_3 nanoplatelet across its phase transition.

Chapter 2

Methods

2.1 Device Fabrication

2.1.1 Crystal Growth and Transfer

We grow single-crystal VO_2 nanobeams [33] in a three-zone furnace manufactured by Protherm. V_2O_5 powder is used as a precursor and the substrate is a (100) Si chip covered by 1 μm thick SiO_2 layer. The growth is divided into two parts. During the first period, the furnace is put under vacuum (10^{-2} mbar) and heated up to 780 °C from room temperature in ~20 minutes, then oxygen gas is supplied into the chamber at 0.5 sccm. In the meantime, V_2O_5 droplets vaporize and condense on to the substrate surface. As soon as the furnace reaches the target temperature, oxygen flow is cut and the chamber is kept at the target temperature for 90 minutes, while the V_2O_5 domes start forming the VO_2 nanobeams. The following reaction is proposed for the growth [34]:

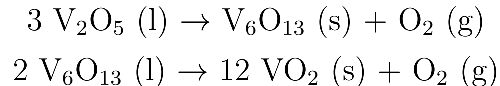

$$3\ V_2O_5\ (l) \rightarrow V_6O_{13}\ (s) + O_2\ (g)$$
$$2\ V_6O_{13}\ (l) \rightarrow 12\ VO_2\ (s) + O_2\ (g)$$

The nanobeams typically have a high aspect ratio in order to provide a bridge-type Hall-bar geometry. Crystals are picked up from the substrate with an ultra-sharp needle controlled by a micromanipulator, and then transferred on to h-BN flakes. This method releases the stress caused by adhesion to the substrate, and creates free-standing crystals [31]. With the help of ion milling, VO_2 crystals are thinned down from ∼100 to 4-6 nm and shaped into desired device structure in a controlled manner (see ‘Argon and Gallium ion milling’ - section 2.1.2).

The V_2O_3 nanoplatelets mentioned in this work are grown in a custom made furnace that provides real-time optical observation capability [35]. We rely on a salt-assisted CVD method where Potassium Iodide (KI) salt is used. The chamber is first brought to vacuum (10^{-3} mbar) and filled with Ar at atmospheric pressure. As KI:V_2O_5 mixture starts melting when the chamber reaches 660 °C, H_2 gas flows into the chamber and temperature is ramped up to 850 °C. KI salt reacts with V_2O_5 at elevated temperatures to form potassium vanadate (KV_3O_8). Then, KV_3O_8 is reduced to V_2O_3 by the following chemical reaction:

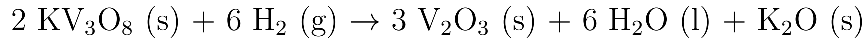

$$2\ \mathrm{KV_3O_8}\ (s) + 6\ \mathrm{H_2}\ (g) \rightarrow 3\ \mathrm{V_2O_3}\ (s) + 6\ \mathrm{H_2O}\ (l) + \mathrm{K_2O}\ (s)$$

The nanoplatelets can grow as large as 2-3 μm thickness-wise, though thin ones down to ∼10 nm can be found. The nanoplatelets are found to have layered structure with non-van der Waals stacking [26], as shown in Figure 2.1.

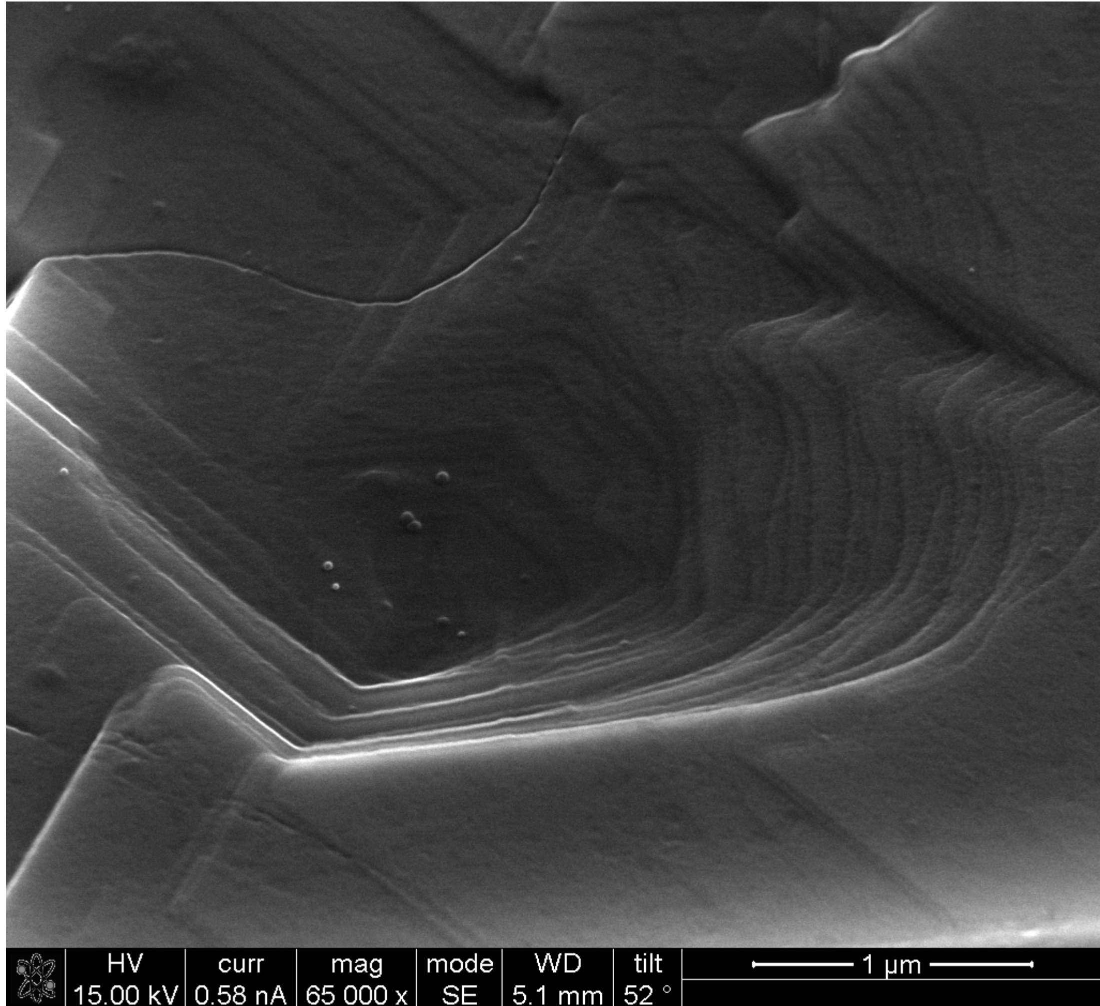

Figure 2.1: SEM micrograph showing the layered nature of the V_2O_3 nanoplatelet.

2.1.2 Argon and Gallium ion milling

We use Gallium ion milling in a Focused Ion Beam (FIB) equipment to shape VO_2/V_2O_3 crystals into Hall-bar structure. One of the advantages of this technique is that the samples are directly imaged and an area on the sample are selectively etched in a single step, rather than requiring separate masking and etching processes. However, as the Ga-ions hit the crystal surface with a high impact energy, some ions will get implanted into the crystal, and over time a damaged layer will form on the crystal surface.

Ga-ions are accelerated at 30 keV beam energy by the ion gun in FIB. An alternative source of ions can be found in an X-ray Photoelectron Spectroscopy (XPS) equipment with Ar-ion etching capability. There, we can set the energy of Ar-ions to be 1 keV. We show in the results section (see 'Ion damage analysis in crystal shaping' - section 3.1) that Ga-ions penetrate 20 nm from the surface of a VO_2 crystal. On the other hand, the damaged layer left by etching with Ar-ions is at 5.2 nm from the surface. Since the incident ion energy is a significant parameter for the ion penetration depth, the smaller energy of Ar-ions would be less damaging to the crystal surface. Furthermore, there is an angle of incidence for the Ar-ions of 32° inside the XPS chamber. Thus only the perpendicular component of the impact energy is transferred to the sample. In the final step, the damaged layer which is left by Ar-ion etching is removed by dipping the sample in 37% HCl solution for a few seconds, while the pristine part of the crystal remains unaffected [32].

To fabricate a VO_2/V_2O_3 Hall-bar device, we use both of these etching processes. First, the crystals are shaped into the Hall-bar geometry with Ga-ion etching in FIB (Figure 2.2a). In this step a small portion on top of the crystal, about 20-25 nm, is etched for a crystal of thickness about 100 nm. We terminate Ga-ion etching at this level since further implantation of Ga into the depths of the crystal would be undesirable. We continue milling the crystal with Ar-ion etching (Figure 2.2b), where its thickness is controllably reduced to about 10 nm. This step would completely remove the implanted Ga-ions in the first place, as the maximum depth of Ga implantation is found to be 20 nm. Finally, the amorphous film that is induced by Ar-ion etching is removed with HCl treatment (Figure 2.2c). Another advantage of reducing the thickness of VO_2 crystals is found to be minimizing the chance of cracking during the MIT (see 'Cracking crystals during heating' - section 3.2). In the light of these results, we report here a technique that would enable to shape VO_2/V_2O_3 into Hall-bar geometry and also preserve the pristine electrical and mechanical properties of the crystals.

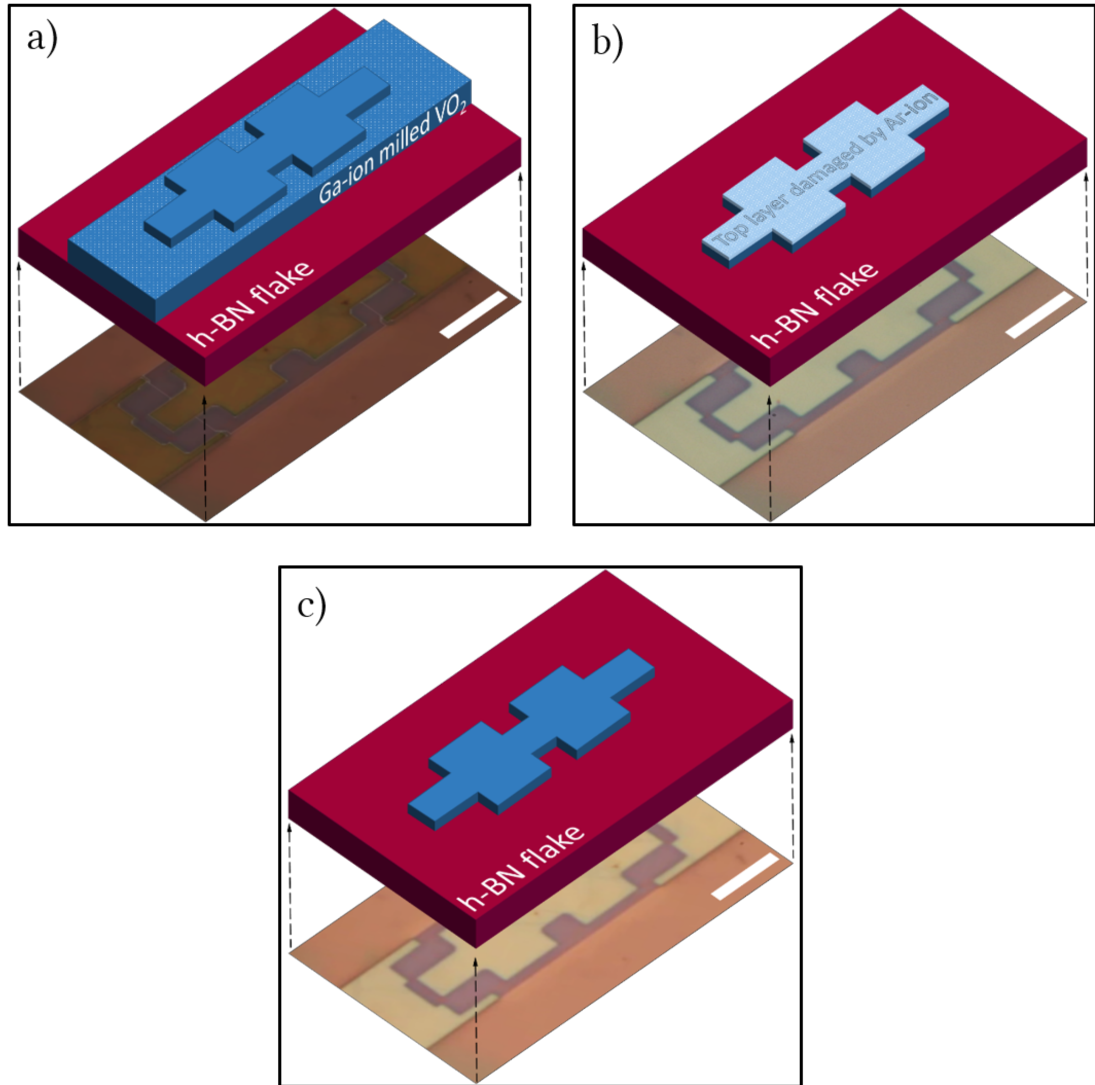

Figure 2.2: **a** Shaping the crystal into the bridge-type Hall-bar geometry via Ga-ion milling. The ions only etch a small portion on top of the crystal. **b** The crystal is thinned down from ∼100 nm to 10 nm via Ar-ion milling. **c** The crystal is treated with HCl or BOE solution to remove the amorphous layer left by Ar-ion milling. This step restores the electrical properties of the crystal to a pristine form [32]. Each scalebar represents 10 μm.

2.1.3 E-beam lithography

The patterning of VO_2 and V_2O_3 devices in this work required a two-step electron beam lithography process. Provided that the crystal to be patterned rests on a rectangular shaped wafer with at least one flat side and a sharp corner, we first determine the position of the crystal on the wafer with respect to an origin point down to the precision of a few tens of microns. A digital on-screen ruler application named 'MB-Ruler' and an optical microscope with a live-view camera system is utilized as shown in Figure 2.3.

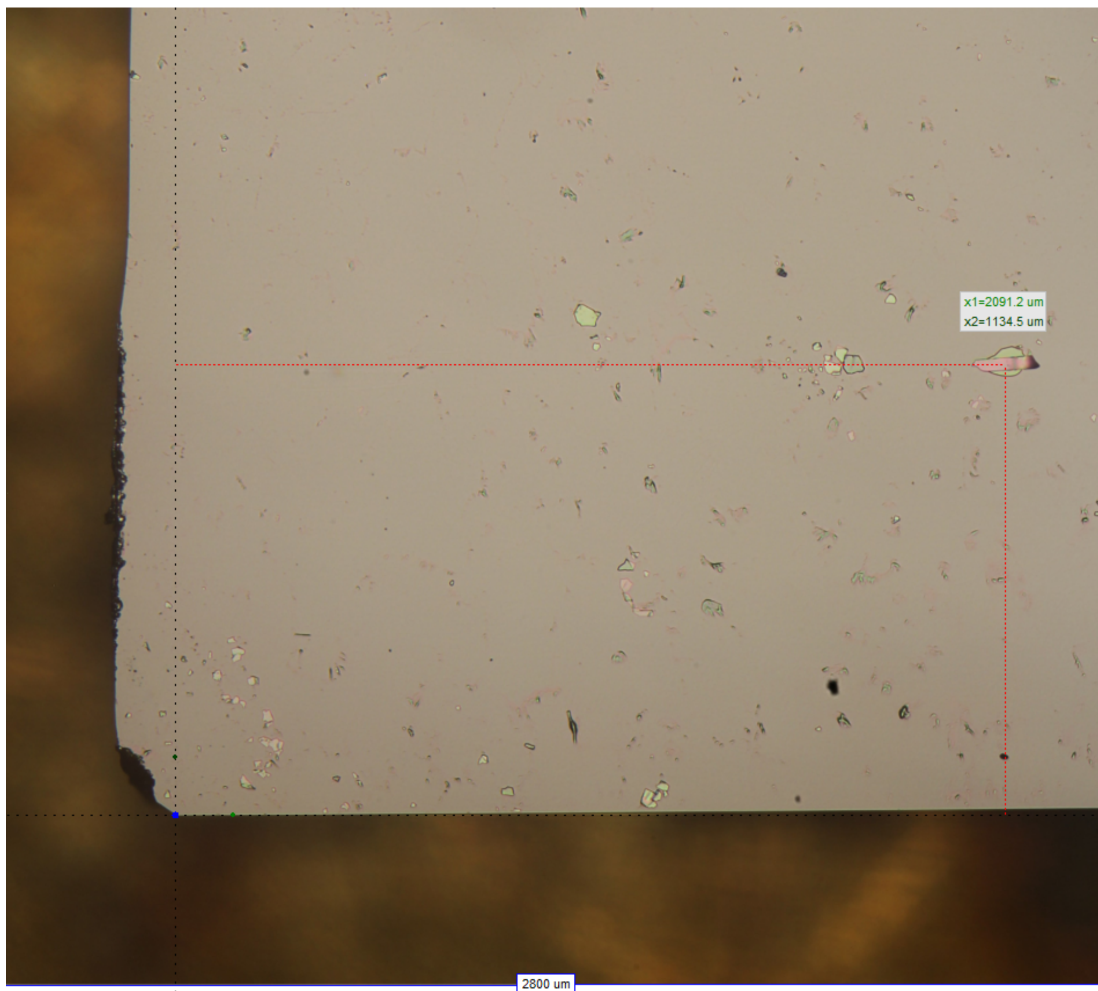

Figure 2.3: The live-view camera system for determining the coordinates of a crystal on the wafer.

The next step includes the spin coating of the samples with a double-layer

Poly(methyl methacrylate) resist (PMMA). The samples get washed with Acetone + IPA + DI water and are mildly flushed with nitrogen gas in order to get rid of dirt and dust particles that accumulate on the surface. Then as the first layer of resist, 2-3 droplets of 495 K PMMA A6 is dropped onto the surface of the sample with a glass pipette. The spinning process starts at 500 rpm with an acceleration of 250 rpm which goes on for the first 5 seconds, then the rotation gradually increases to 3000 rpm and lasts for another 35 seconds. Following this the sample gets baked on a hot-plate at 180 °C for 2 minutes. The first layer of coating leaves a resist thickness of 380 nm. The spin coating process resumes with the next layer of resist; 950 K PMMA A6 which is coated and baked by following the same recipe as the first layer. This step adds to the resist thickness by about 290 nm, so the total film thickness becomes 670 nm (see 'Atomic Force Microscopy' - section 2.2.1). The purpose of the double-layer coating is to achieve an undercut profile of the side-walls of electrodes, which then provides a proper lift-off after the metal evaporation procedure is performed.

The aforementioned coating method is sufficient to pattern a crystal that rests on a normal or prime quality SiO_2 wafer, such being the case for all VO_2 devices that have been investigated in this work. In contrast, some of the V_2O_3 devices were patterned on a sapphire substrate which has a highly insulating nature. To prevent e-beam patterning defects on those structures, we have coated a layer of conductive polymer such as poly(3,4-ethylenedioxythiophene) polystyrene sulfonate (PEDOT:PSS) underneath the PMMA layers.

As the first step of the lithography procedure, a square shaped area (optical image shown in Figure 2.4) which contains the orientation indicators and alignment crosses has to be patterned in the vicinity of the crystal. Since the sample cannot be imaged by the electron microscope after it is coated with the resist, we use these alignment marks to match the contact design with the device. Our e-beam lithography processes are carried out on a 'Nova 600 NanoSEM' electron microscope by the FEI company. The beam parameters are set as the following: the voltage is at 30 kV which provides the maximum penetration depth possible into the resist layer, the beam current is varied between 52 to 230 pA depending on the feature length of the desired pattern and finally the dose is kept at 100

μC/cm^2.

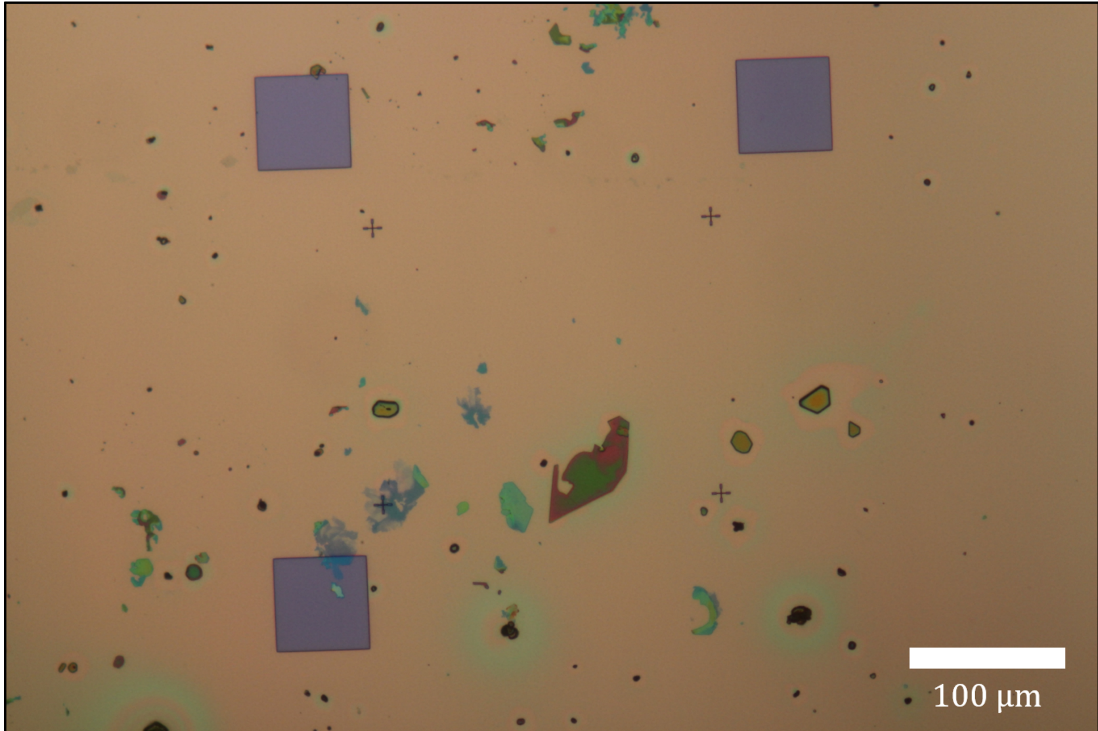

Figure 2.4: The orientation indicators (squares) and alignment marks (crosses) are used to align the crystal with the desired contact pattern.

To develop the exposed regions, we dip the sample in a developer solution which consists of 1:3 MIBK to IPA (Methyl isobutyl ketone and isopropyl alcohol, respectively) for a duration of 65 seconds. The sample is then transferred into an IPA bottle for 15 seconds which acts as the stopper. Finally we rinse the sample in deionized water for $\sim$2-3 seconds and flush with nitrogen gas to get rid of liquid residues.

Following the development of alignment marks, we simply capture an image in an optical microscope and prepare the design of the electrodes in a computer software named 'KLayout' based on the optical image of the sample. The three squares in the alignment mark design serves us to determine the spatial orientation, and the four crosses helps to make necessary adjustments such as shifting/zoom/rotation in order to have a desired match between the prepared design and the patterned device. A typical designing scheme is shown in Figure 2.5.

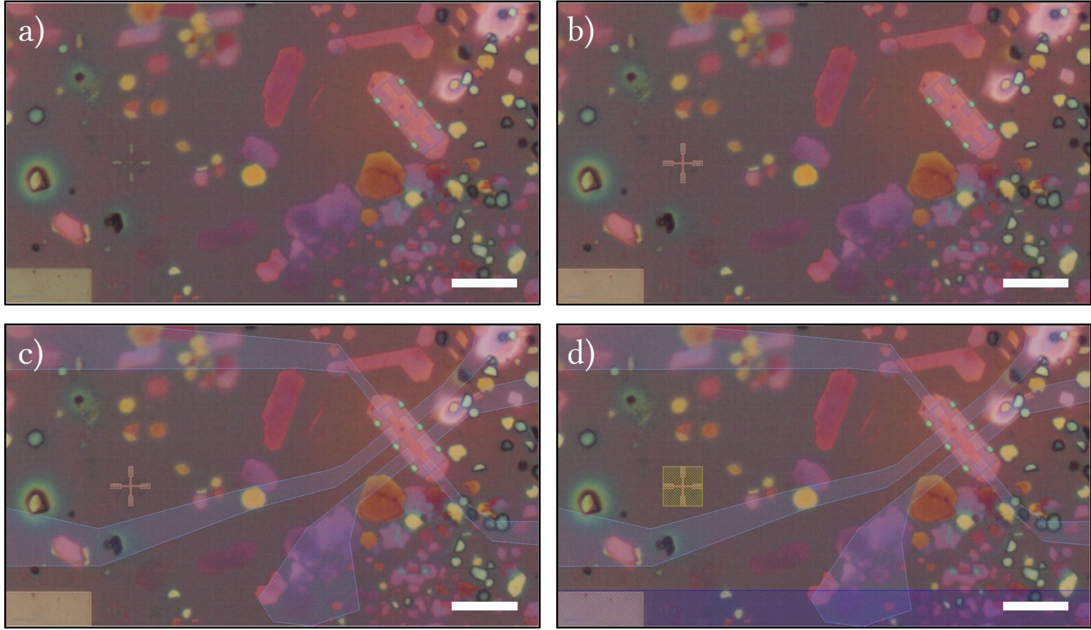

Figure 2.5: The design process starts with outlining the alignment marks as shown in step **b**. Then, the contact regions are designed for the device as shown in **c-d**. Scalebars represent 20 μm.

For the sake of time efficiency, we often design the inner legs that attach to the crystal and the outer pads for wire connections on separate files in order to pattern them at different rates. Since the inner legs typically contain the finer features of the design, it is preferable to keep the electron beam current as low as possible, therefore we usually select 26 or 52 pA beam current. On the contrary, each of the outer pads take up a 300-by-300 μm^2 area, and consequently precision is of secondary importance rather than patterning duration. In that case the beam current could be set as large as desired to decrease the duration of the patterning.

Finally, the exposed regions of the wafer are developed by the same recipe which we use in developing the alignment marks. A VO_2 Hall-bar patterned on Si substrate and a V_2O_3 Hall-bar patterned on a sapphire substrate are shown in Figure 2.6. Immediately after the final development, we keep the samples inside an argon glovebox to prevent oxidation of the exposed regions.

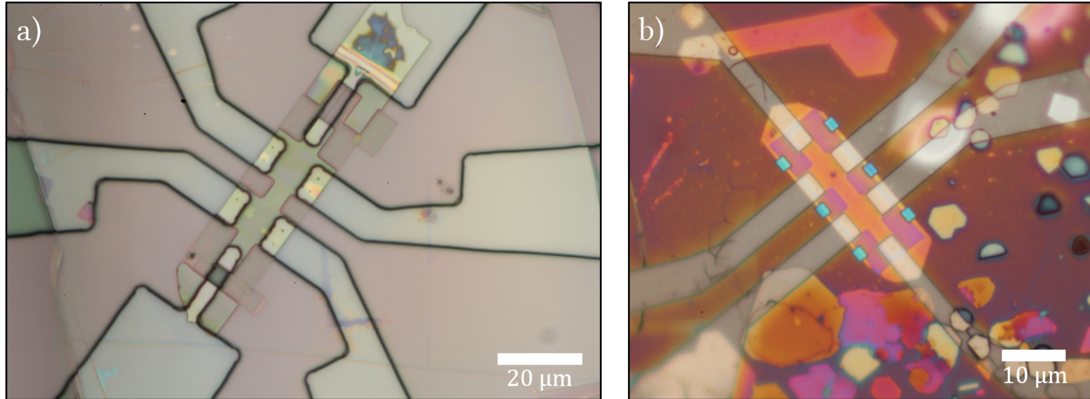

Figure 2.6: **a** VO_2 and **b** V_2O_3 Hall-bars with the contact regions developed for metal evaporation.

2.1.4 Metal Contact Evaporation and Wire Bonding

Although the patterned devices are always kept inside the glovebox, the surface of some of the VO_2/V_2O_3 devices get oxidized, which severely affects the device performance. To eliminate this problem, we dip the samples in a buffered oxide etch (BOE) solution just before the metal contact evaporation process. BOE only attacks to the oxidized layer and leaves a pristine surface on VO_2/V_2O_3 (See 'Atomic Force Microscopy' - section 2.2.1). As soon as the BOE treatment is done, we thermally evaporate about 100/5 nm thick Au/Cr layer on the samples. An example of evaporated VO_2 and V_2O_3 devices are given in Figure 2.7. The evaporated samples are kept in hot acetone bath (60 °C) for 5 minutes for the lift-off process.

We use a 4524AD Series Manual Wire Bonder by Kulicke & Soffa Dicing Systems. The equipment is utilized in ball-bonding mode where each terminal of a device is bonded to a 6-pin sample chip that fits into the PPMS stage. As a standard method, the wire bonder stage is usually heated up to ease the sticking of the gold wire to the surface of the sample, but our devices are prone to cracking above a certain temperature, thus we bond the gold wires at room temperature. As a result, a larger amount of force is applied to stick the wire on to the contact surface, however too much force may also result in breaking the metal contacts of the device.

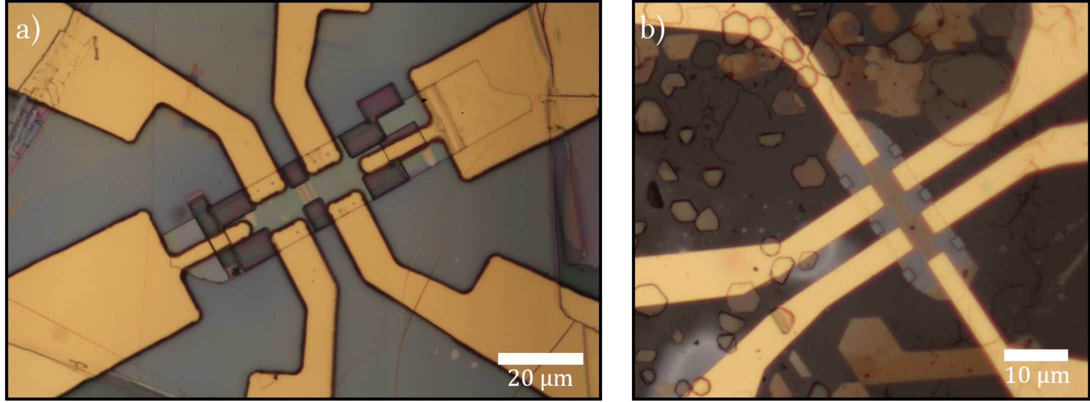

Figure 2.7: Au/Cr contacts deposited onto the devices from Figure 2.6

2.2 Characterization

2.2.1 Atomic Force Microscopy

We used contact-mode Atomic Force Microscopy (AFM) to determine the thickness of PMMA layer coating for the e-beam lithography process. It is found that double layer coating of 495 K PMMA A6 and 950 K PMMA A6 gives the thickest coating (Table 2.1), which produced the highest yield for metal contact evaporation.

	Softbake (mins)	Thickness (nm)
495 K A4	2	320
495 K A6	2	**380**
495 K A6	10	390
950 K A2	2	85
950 K A6	2	**350**
495 K A6 + 950 K A6	2 + 2	**670**

Table 2.1: Thickness data of various PMMA coating recipes. The rotation speed is 3000 rpm and duration is 40 seconds for each step. Thickness data in bold represents the recipes used in this work.

A 5 second dipping of an oxidized V_2O_3 crystal into the BOE solution (6:1 volume ratio of 40% NH_4F:49% HF in water) results in reduction of the V_2O_3 sample thickness by 7 nm. A dip of 15 seconds in BOE does not show any further reduction in the thickness. Therefore we conclude that the oxide layer is around 7 nm in the V_2O_3 nanoplatelet (Figure 2.8). More than 5 seconds of dipping increases the roughness of the surface, though we have not noticed a negative impact to the device performance because of this.

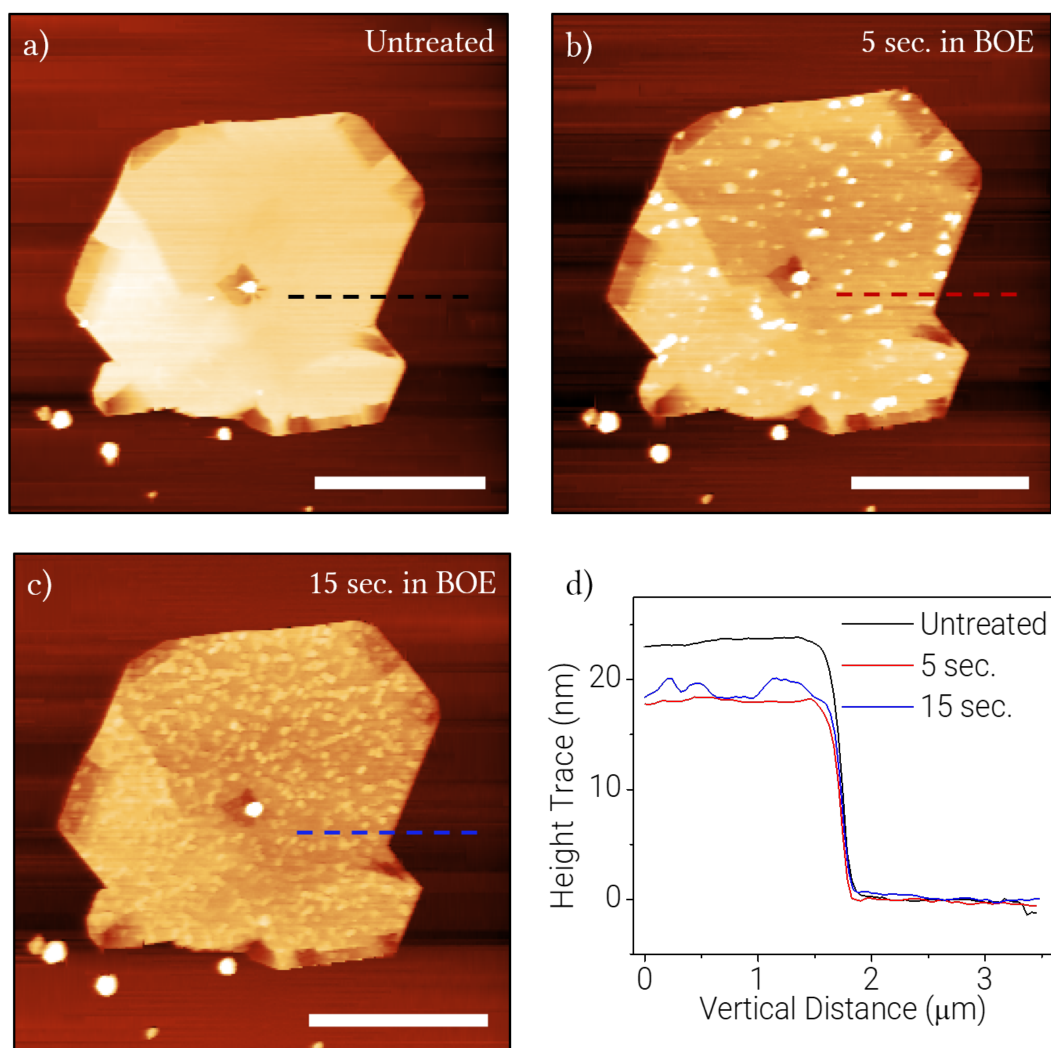

Figure 2.8: BOE treatment reduces the thickness sample by 7 nm in 5 seconds dip. A further 15 seconds of dipping does not change the thickness, thus the oxide layer is completely removed from the sample. Each scalebar represents 4 μm.

Chapter 3

Results and Discussion

3.1 Ion damage analysis in crystal shaping

The formation of the amorphous layer is introduced by the ion-beam induced damage on the VO_2 and V_2O_3 crystals. We used the software SRIM-2013 (Stopping and Range of Ions in Matter) by *Ziegler et al.* [36] to analyze the range of Ga and Ar-ions that hit the crystal surface. The analysis software is based on the method of binary collision approximation, to simulate the Ga and Ar-ion damage effect. To replicate milling process we used on shaping the crystals into Hall-bar structure, Ga-ions are targeted to the surface at 0° from the normal with an energy of 30 keV. Figure 3.1 shows the depth of ion penetration with respect to the number of ions that hit the surface. Ga-ions quickly reach 14 nm of depth from the surface of the crystal, and over time as more ions are sent the penetration saturates at 20 nm.

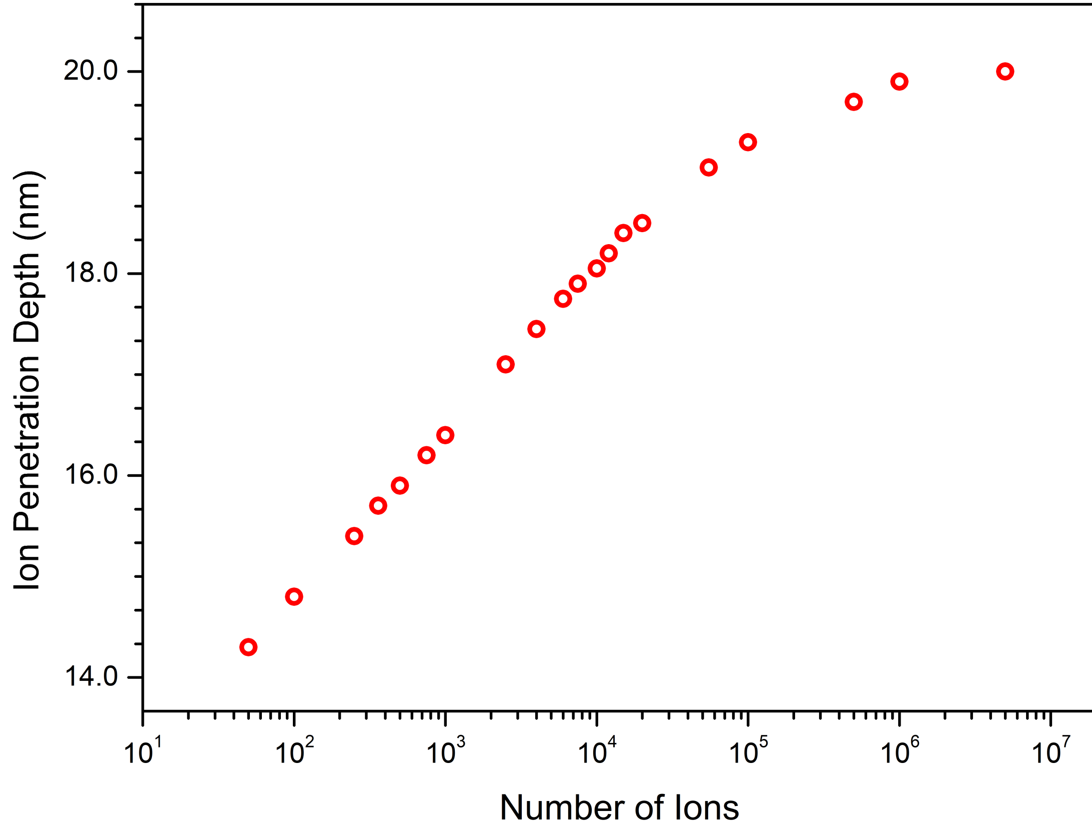

Figure 3.1: SRIM results showing the Ga-ion damage on the VO_2 crystal with increasing number of ions. The maximum depth of implanted ions converge to 20 nm from the surface of the crystal.

To simulate the Ar-ion beam damage effect, we target Ar-ions to the surface by 32° from the normal and with an energy of 1 keV. Figure 3.2 demonstrates the range of Ar-ions inside the VO_2 crystal. In contrast to Ga-ion milling, Ar-ions leave about 5.2 nm of a damaged layer on the surface of the crystal. We infer from the results that only logarithmic increments in the number of ions result in a similar increase in penetration depth, thus the beam induced damage on the crystal builds up at a decelerating rate. There are two limiting parameters that can be stated about the event; firstly, we provide relatively small energy compared to what ion penetration requires in order to cause damage on the surface film of the crystal. In addition, the sputtering of the surface atoms reduce the thickness of the amorphous film even though the penetration depth increases.

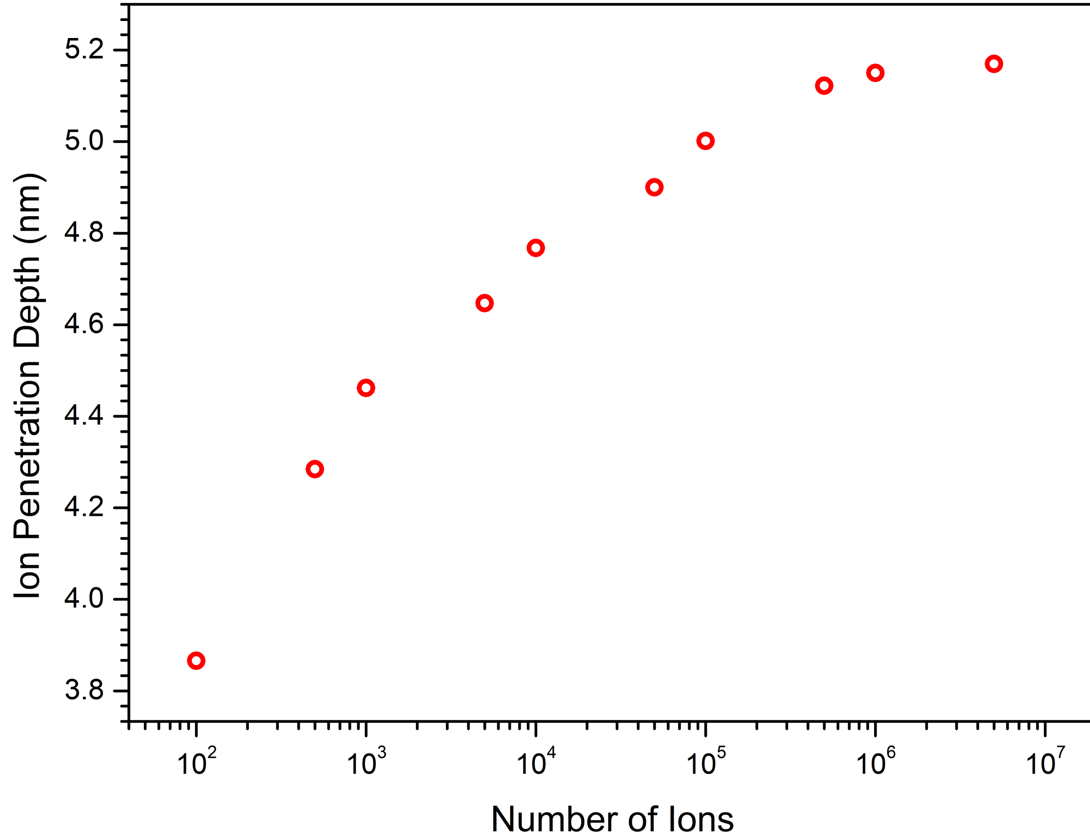

Figure 3.2: SRIM results showing the Ar-ion damage on the VO_2 crystal with increasing number of ions. The maximum depth of implanted ions converge to 5.2 nm from the surface of the crystal.

Figure 3.3 displays the simulated evolution of the ion distribution in the crystal. Fluence, which is defined as the ratio of target density to the ion dose, is shown on the y-axis of the plots. We observe that most of the Ar-ions are concentrated at 1.7 nm from the surface of the crystal. This is where the majority of the damage is done. The density of implanted ions decrease exponentially towards the maximum depth of 5.2 nm. As a result of this, the oxygen-poor Magnéli phases (a mixed state of VO and VO_2) might be located in this range of the crystal.

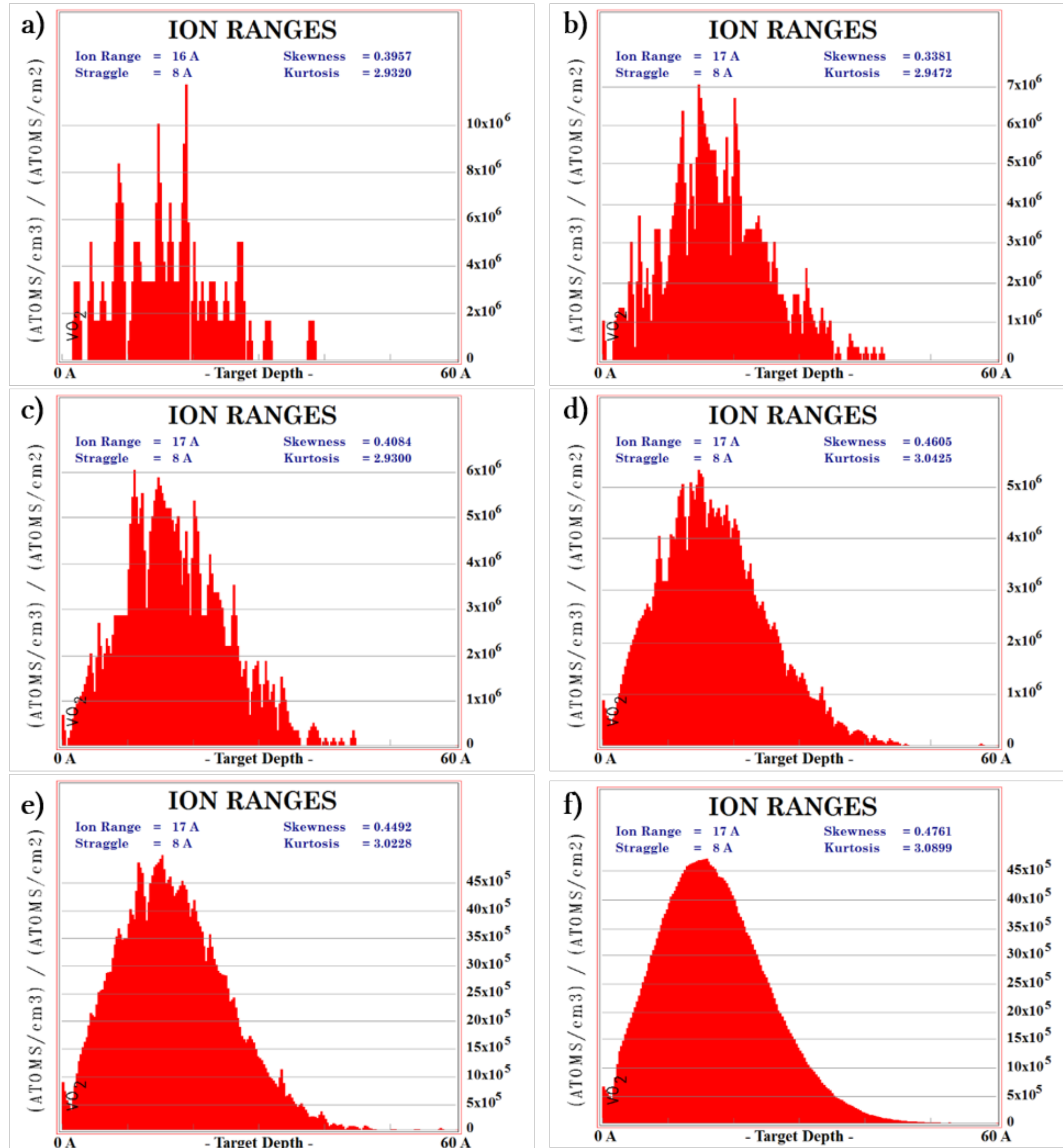

Figure 3.3: Evolution of the Ar-ion distribution in the VO_2 crystal. Majority of the ions are located at 1.7 nm from the surface of the crystal.

Following the ion range simulations, we have looked at the cross-sectional view of two Ar-ion etched VO_2 crystals in a High-Resolution Transmission Electron Microscope (HR-TEM), one etched for 10 minutes (Figure 3.4a) and the other for 40 minutes (Figure 3.4b). The damaged layer is indicated between the dashed lines. In both cases, the amorphous layer is observed to have a thickness of 5.6

nm. This is in agreement with our simulation results.

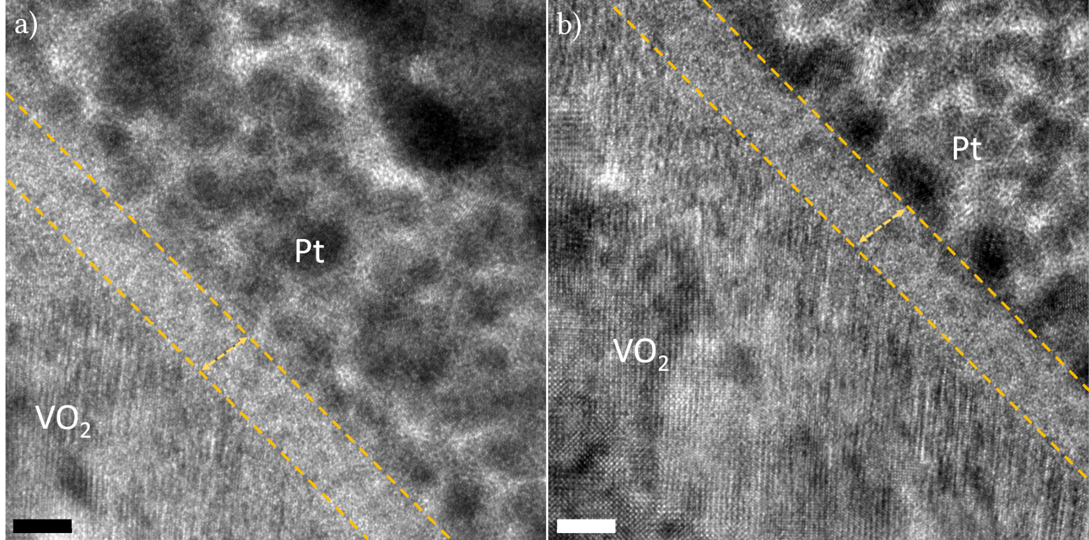

Figure 3.4: HR-TEM image showing a cross-section of **a.** 10 minutes and **b.** 40 minutes Ar-ion etched VO_2 nanobeams. The thickness of the amorphous layer, represented by yellow dashed lines, is found to be 5.6 nm. Each scalebar represent 5 nm. Taken from ref. [32].

We have shown on a previous work that Ar-ion milled VO_2 nanobeams retain their pristine electrical properties after the damaged layer is removed from the crystal with a dip in HCl [32], as shown in Figure 3.5. Here, we compare the resistance of a pristine, Ar-ion etched and HCl treated VO_2 device across its MIT. Considering the untreated etched state of the device, the decrease in the change of resistance across the MIT is attributed to the formation of the amorphous layer. Upon 1 minute of HCl treatment, we observe that the electrical properties of the device is restored to the pristine form.

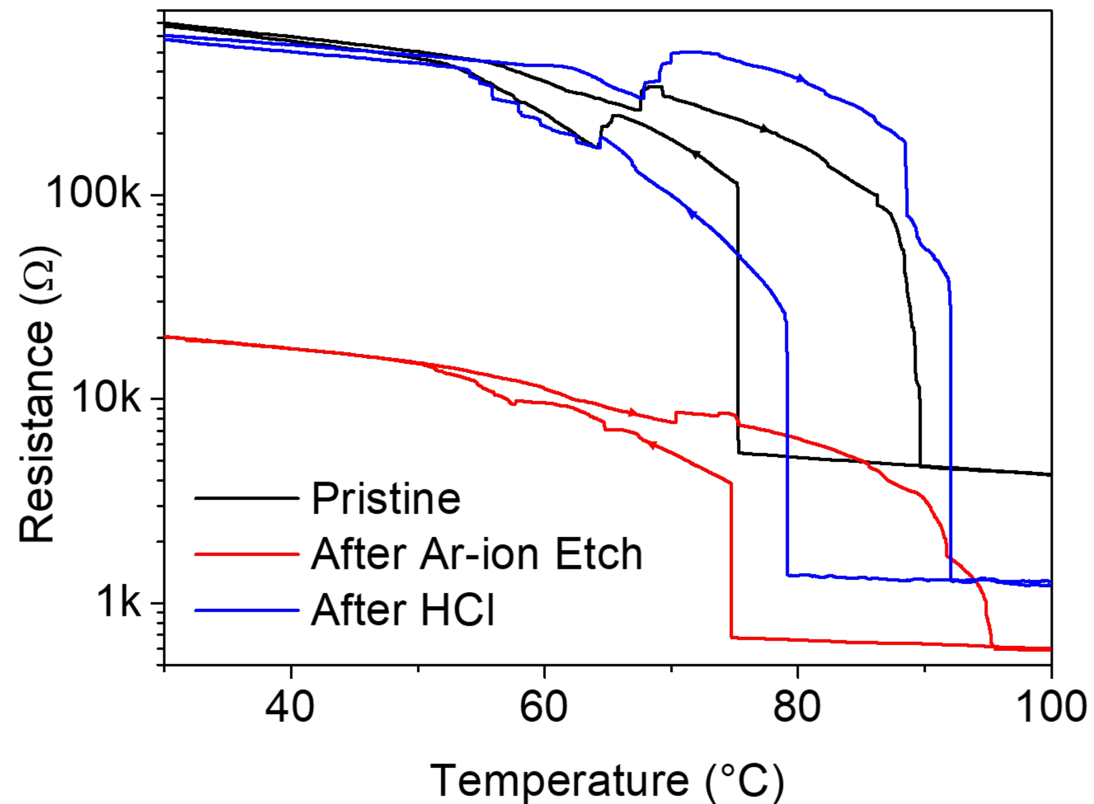

Figure 3.5: Resistance vs temperature cycle of pristine, milled and HCl treated VO_2. The milled VO_2 has reduced resistance response due to being in series connection with the ion-beam induced damaged layer. The nanobeam retrieves its pristine electrical properties after HCl treatment. Taken from ref. [32].

3.2 Cracking crystals during heating

We have observed that when we shape the as-grown VO_2 nanobeams into Hall-bar structure, the crystals began cracking as they undergo MIT. The cracks mostly arise from the shaped corners of the Hall-bar structure, where the device is structurally weaker.

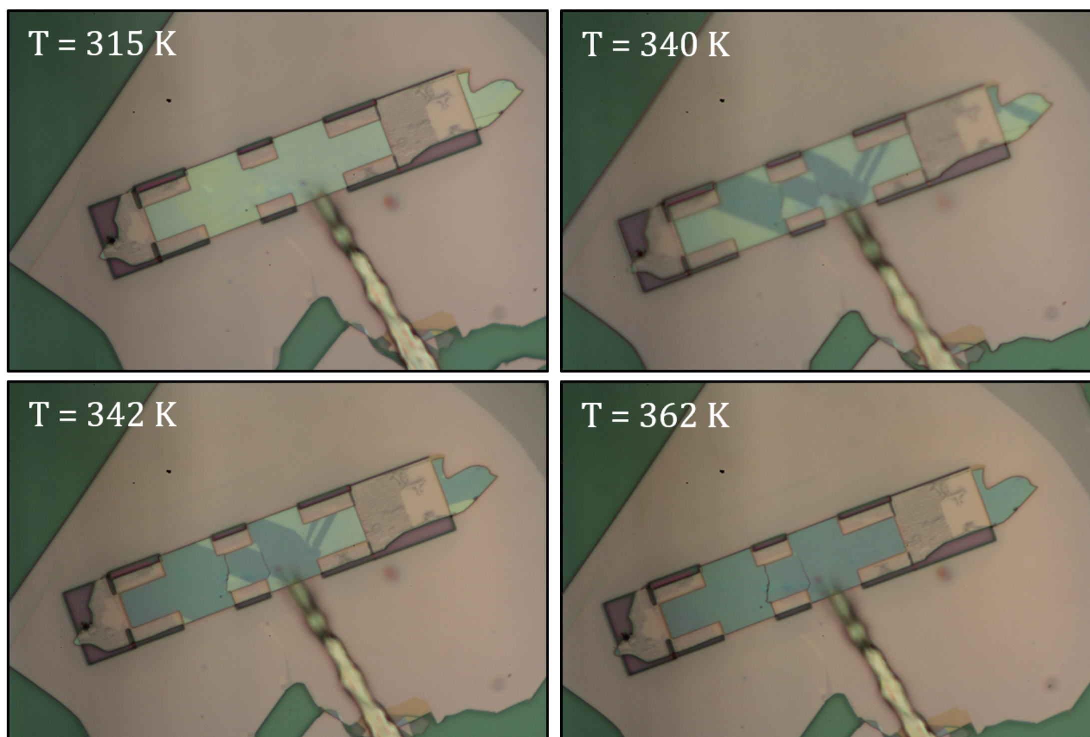

Figure 3.6: Two cracks appear on a 160 nm thick Hall-bar shaped VO_2 crystal during the MIT as a result of the stress introduced by the structural phase transition.

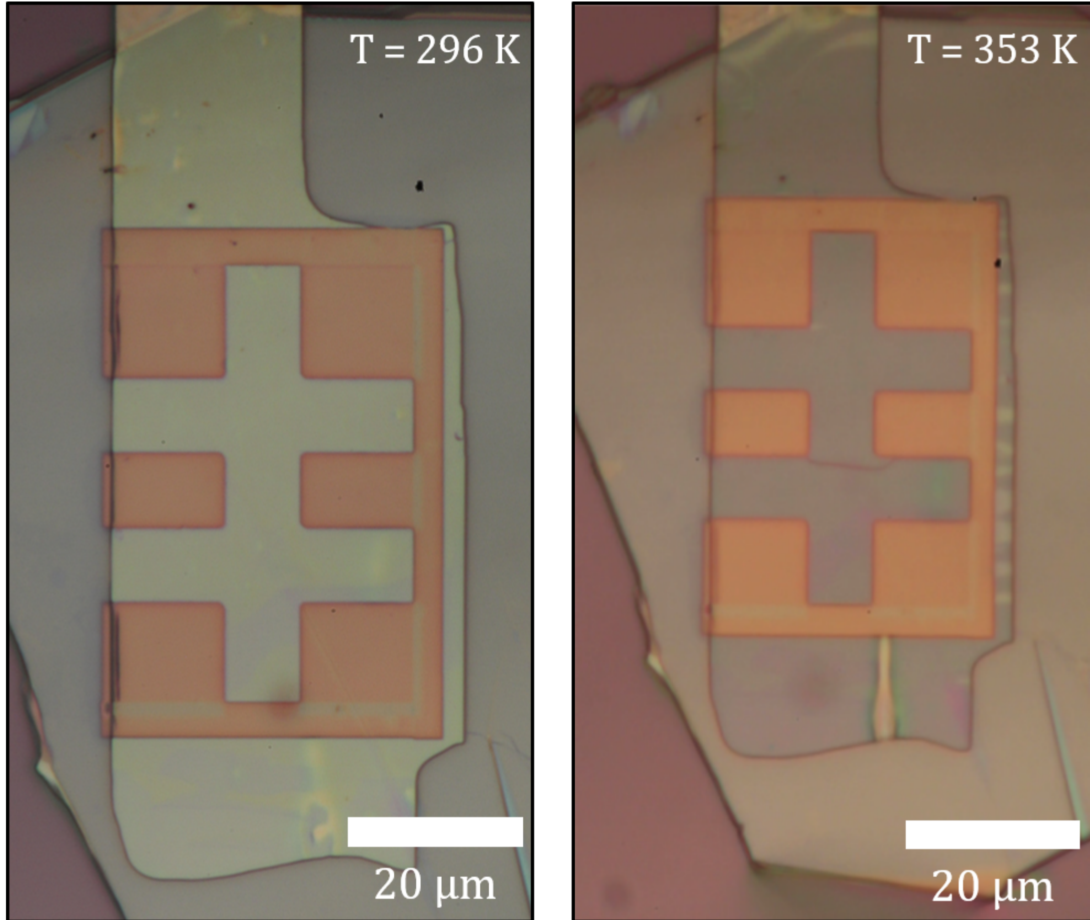

Figure 3.7: A 174 nm thick VO_2 crystal shaped into Hall-bar geometry cracks during the MIT as a result of the stress introduced by the structural phase transition.

A significant source of strain would come from the CVD grown VO_2 beams attaching to the substrate surface. As the temperature increases in the system, the crystal and the substrate try to expand at different rates, which results in non-uniform stress building on the VO_2. To eliminate this, transferring the VO_2 nanobeam on an atomically flat surface such as an h-BN plate proved to reduce the non-uniform stress on the nanobeam [37]. Even then, we have observed that thicker crystals (above 50-100 nm thickness) tend to crack after being shaped into Hall-bar structures (Figures 3.6 and 3.7). Therefore, we have tried to increase the elasticity of the crystals by reducing their thickness. We used Ar-ion milling

to thin down VO_2 Hall-bars to ~10 nm thicknesses with a controlled etch rate. The VO_2 crystals shown in Figure 3.8 and 3.9 have successfully demonstrated the MIT without any crack appearing on the crystals. We could deduce that the crystals are free-standing because 1) the transition begins near the expected temperature for free-standing crystals (338 K [14]) and 2) fewer phase separated regions occur as the transition is taking place.

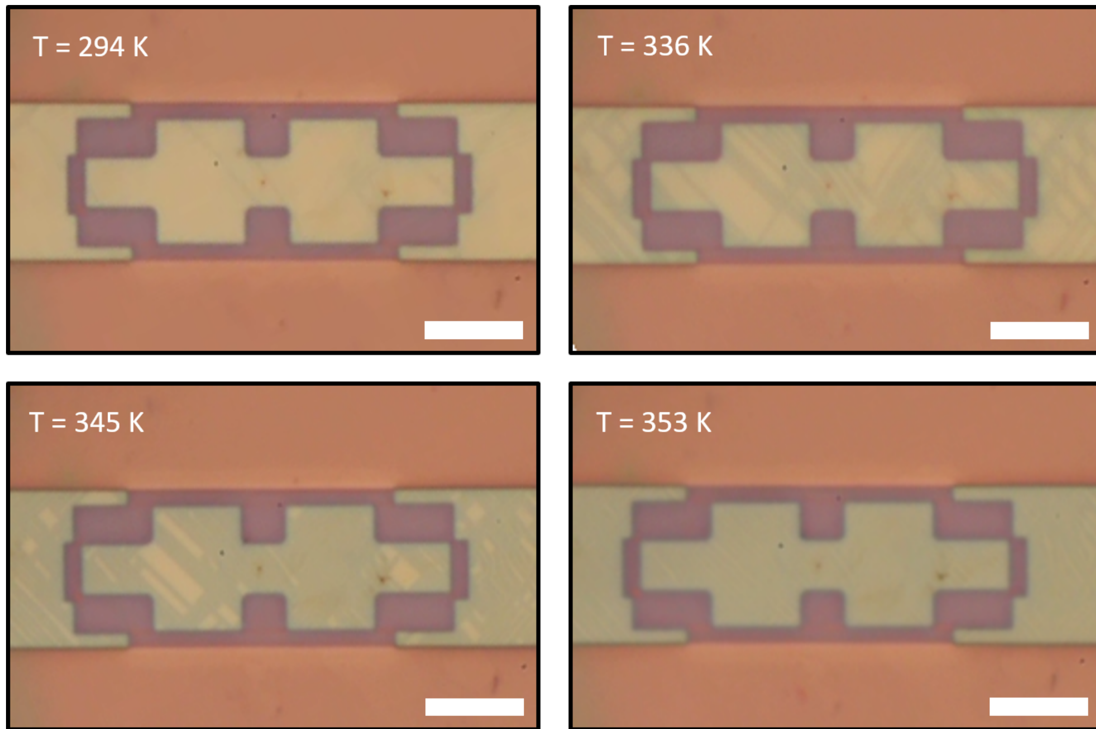

Figure 3.8: Successful insulator-to-metal transition of a Hall-bar shaped VO_2 crystal. The crystal is thinned down to 10 nm thickness and treated with HCl to remove the amorphous surface layer. The transition starts taking place near the expected temperature for free-standing crystals (338 K [14]). Each scalebar represents 10 µm.

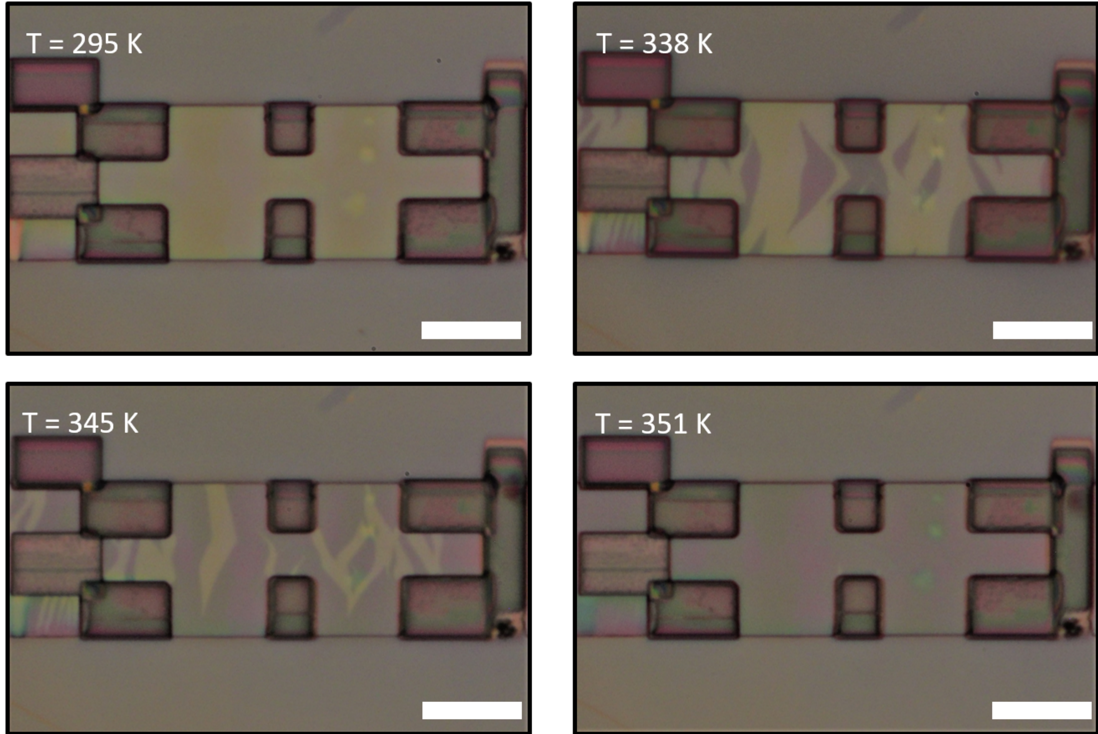

Figure 3.9: Successful insulator-to-metal transition of a Hall-bar shaped VO_2 crystal. The crystal is thinned down to 10 nm thickness and treated with HCl to remove the amorphous surface layer. The transition starts taking place near the expected temperature for free-standing crystals (338 K [14]). Each scalebar represents 10 µm.

3.3 Occasions of Device Failure

Due to some wiring defects in our Hall effect measurement setup, very frequently we would fail to achieve a ubiquitous ground level for all the connections in the measurement probe, and as a consequence many devices we have produced have failed as soon as they are loaded inside the measurement chamber. Figure 3.10 shows some of these failed devices.

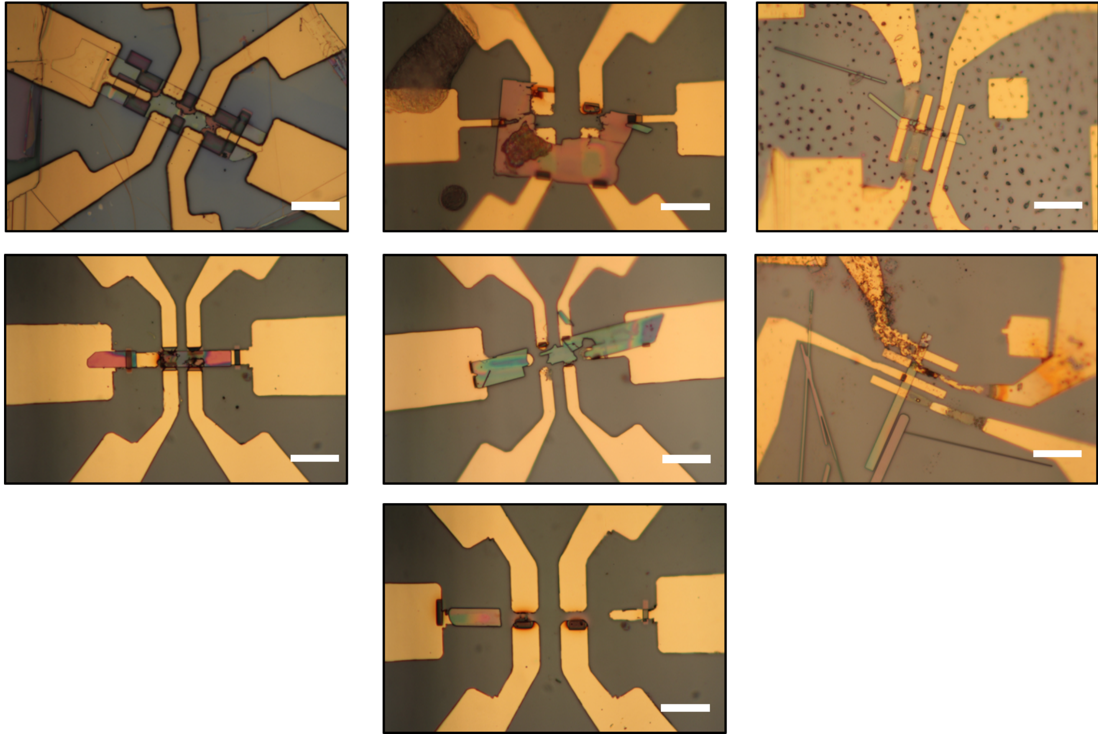

Figure 3.10: Exploded Hall-bar and 4-terminal devices during electrical measurements. Scalebars represent 20 μm.

3.4 VO_2 Measurements

We investigated the resistivity behavior and magnetic response of a 119 nm thick VO_2 nanobeam between 120-300 K. The optical image of the 4-terminal device is given in Figure 3.11.

Figure 3.11: Optical image of a 4-terminal VO_2 device used in magnetoresistance measurements.

The resistivity vs. temperature curve of the device was in agreement with the literature [25]. We observed that VO_2 does not show a phase transition and stays in the M1 phase across the 120-300 K temperature range. The resistivity of this phase depends on the temperature with an Arrhenius type of relation, which is given by:

$$\rho(T) = \rho_0 e^{E_A/k_b T} \tag{3.1}$$

where k_b is the Boltzmann constant and E_a is the activation energy. During the heating cycle, we lost the signal from the device as the temperature reached 225 K, therefore resistivity data above that range is not displayed in Figure 3.12.

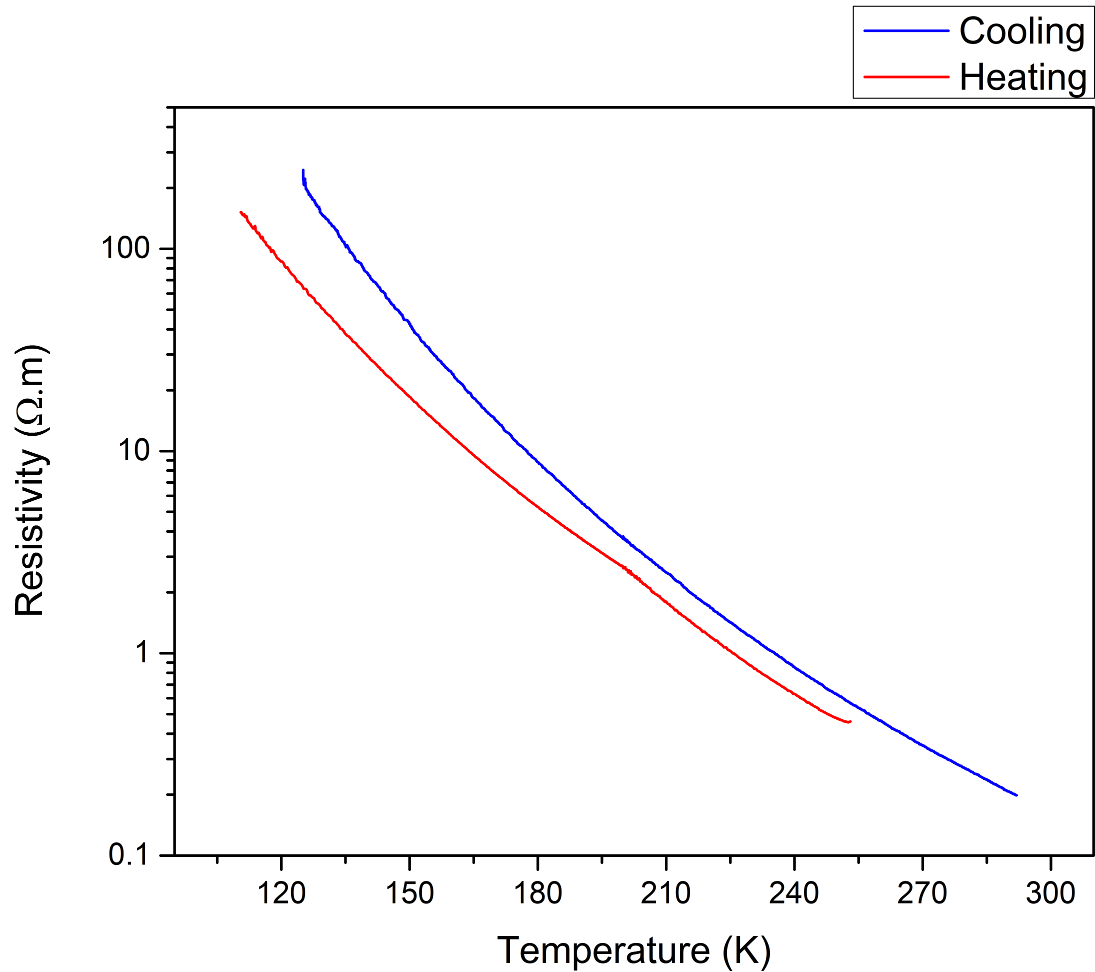

Figure 3.12: Resistivity vs. temperature curve of the 119 nm thick VO_2 device. The device failed while it reached 255 K during the heating cycle.

We applied a perpendicular magnetic field to the device as the temperature is kept at 100 K. The resistance of the device showed no response to the magnetic field up to ± 10 Tesla.

Reports in the literature show that VO_2 is a highly magnetoresistive material even at room temperature [20],[10]. Therefore, even larger magnetic fields are necessary if a Hall measurement is to be performed on VO_2 at lower temperature ranges.

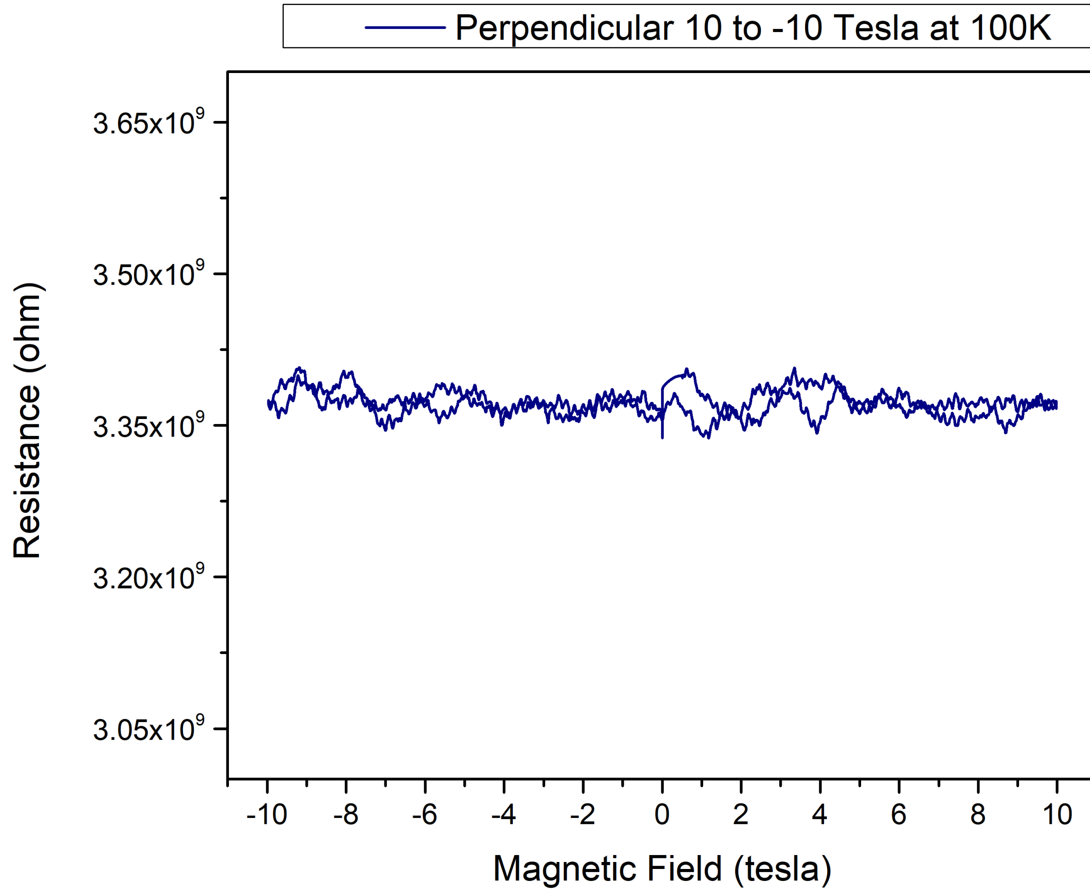

Figure 3.13: The change in the resistance of the device with response to perpendicularly applied magnetic field. Device temperature is kept at 100 K.

3.5 V_2O_3 Measurements

We have fabricated a 6-terminal device of an as-grown V_2O_3 nanoplatelet as shown in 3.14. The purpose of making this device was to observe if the applied magnetic field would have any effect on the device without the crystal being shaped into the Hall-bar structure, compared to a Hall-bar shaped V_2O_3 device.

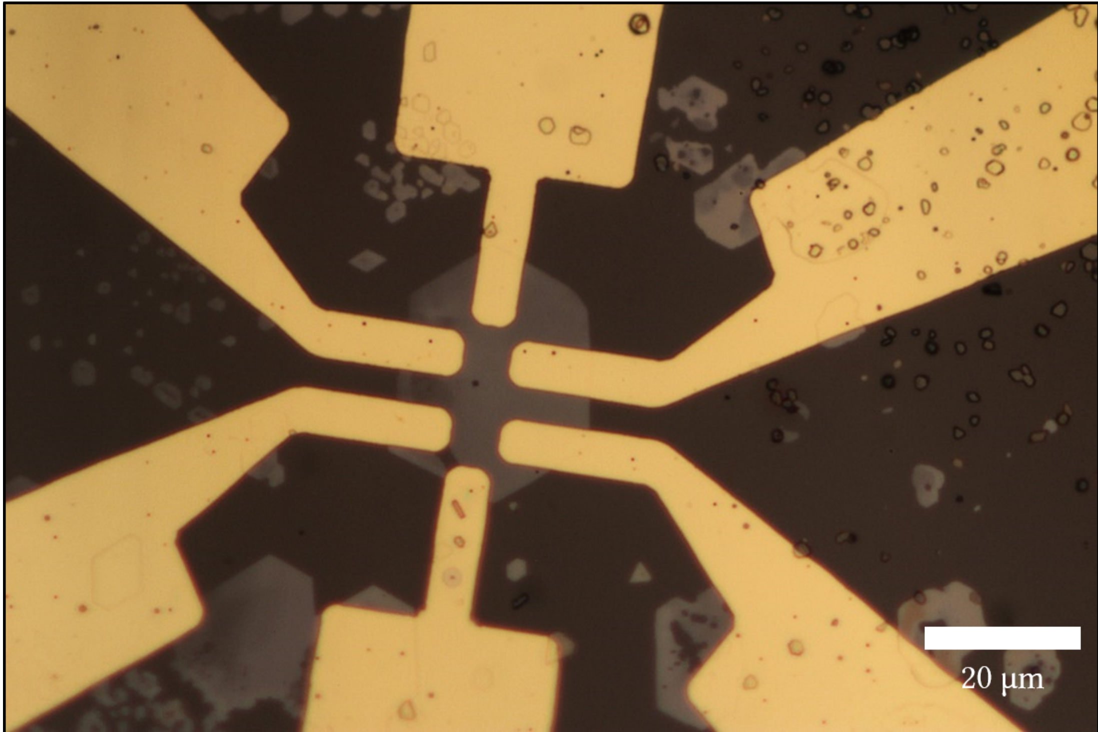

Figure 3.14: Optical image of a 6-terminal V_2O_3 device used to investigate the magnetotransport properties.

The device showed a metal-to-insulator transition around 188 K, which is typical for as-grown samples since the crystal is under tensile stress from adhesion to the substrate (Figure 1.8).

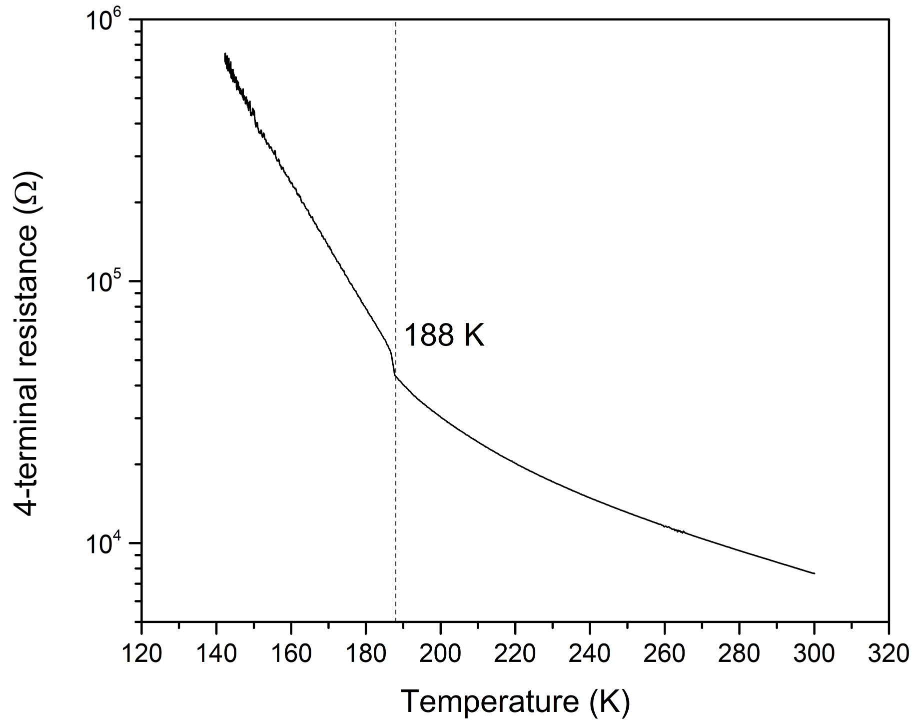

Figure 3.15: Resistance vs. temperature of the V_2O_3 device. A transition from PI to AFI phase of the device is observed at 188 K.

We looked at if any Hall voltage would be generated while the device was either in metallic state (T = 200 K) or insulating state (T = 180 K). We observed that the device did not show a strong response to the perpendicularly applied magnetic field (Figure 3.16). Such a result should be attributed to the absence of a Hall-bar geometry in the device, because the Hall voltage contacts are shorting the Hall voltage. Therefore, a Hall-bar shaped V_2O_3 nanoplatelet device is necessary to extract the carrier concentration and mobility data.

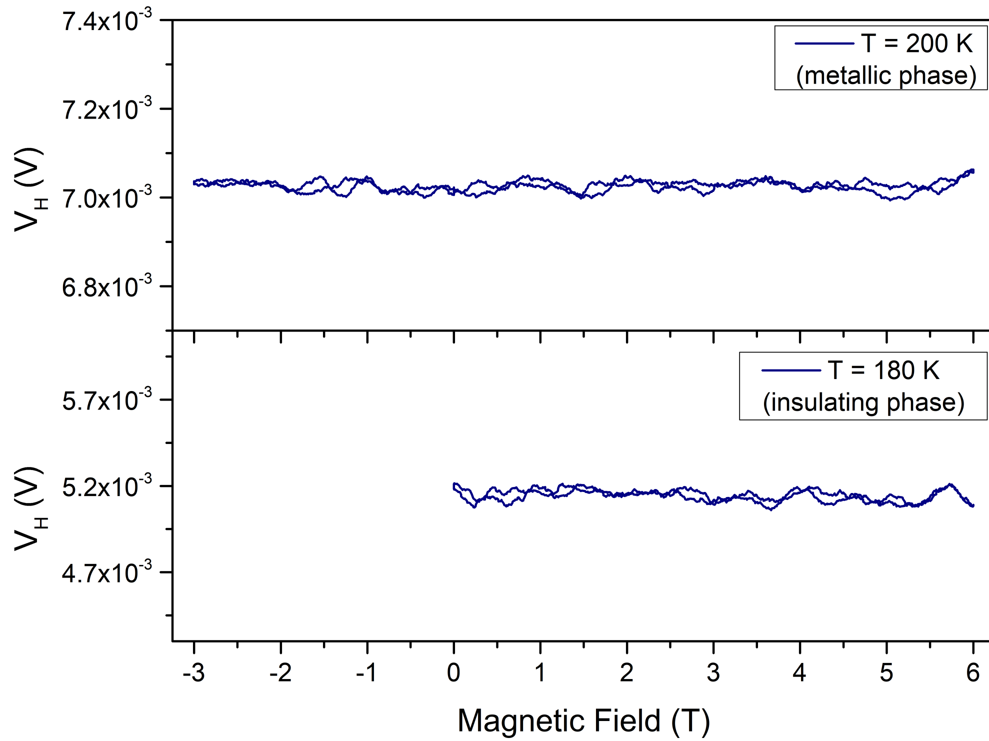

Figure 3.16: The response of the Hall voltage (V_H) to perpendicularly applied magnetic field in PI and AFI phases of the device.

Chapter 4

Conclusions and Future Work

We have successfully observed MIT in shaped VO_2 nanobeams without cracking. Length, width and thickness-wise (after milling down to $\sim$5 nm) the crystals are small enough so that their elastic properties can withstand the structural changes of the phase transition. Our lithography process leaves minimal damage on the crystals, while any remnants of an amorphous structure is eliminated with a dip in HCl. Future aspects of this study are to examine the fundamental transport properties of VO_2 such as carrier density and Hall mobility near its phase transition, as well as in ultra-cold environments. More importantly, with the ion milling techniques we report in this work, VO_2 can be thinned down to a level where the carriers will feel a two-dimensional confinement in their propagation, namely a 2D limit. With that, Hall effect measurements in this regime could bring an exciting prospect to study the effect of two-dimensional confinement in correlated oxide materials.

Aside from Hall effect measurements, the observation of successful MIT in shaped VO_2 can enable new applications for active control of light-matter interactions in nanopolaritonics. Recently, *Dai et al.* [38] have demonstrated that by tuning the local dielectricity of VO_2 via thermally inducing the MIT, the propagation of hyperbolic polaritons in an h-BN/VO_2 heterostructure can be actively

controlled. The tuning of hyperbolic polaritons and their spectroscopic resonances were highly dependent on the geometry of metallic and insulating stripes that appear on the VO_2 crystal as MIT is induced. As we have shown in this work that the occurrence of metallic and insulating regions depend on the stress level of VO_2 (i.e. relatively larger chunks of metallic regions appearing on unshaped VO_2 during the MIT, compared to small and frequent metallic stripes appearing on Hall-bar shaped VO_2 crystals), an h-BN/VO_2 heterostructure that is given a particular shape could enable further tuning for the propagation of hyperbolic polaritons in such devices.

Finally for V_2O_3 devices, external control of parameters such as thickness and strain would give us a deeper understanding about the electrical nature of the crystal. A systematical exfoliation of the layers would bring possibilities to study the Hall effect in V_2O_3 in the 2D regime. Furthermore, by transferring those layers on appropriate substrates that would eliminate the stress on the crystals would be useful to grasp a better understanding of the origin of phase transitions in V_2O_3 crystals.

Bibliography

[1] F. J. Morin, "Oxides Which Show a Metal-to-Insulator Transition at the Neel Temperature," *Phys. Rev. Lett.*, vol. 3, no. 1, pp. 34–36, 1959.

[2] F. H. Chen, "Control of the Metal–Insulator Transition in VO2 Epitaxial Film by Modifying Carrier Density," *ACS Appl. Mater. Interfaces*, vol. 7, pp. 6875–6881, 2015.

[3] N. B. Aetukuri, "Control of the metal-insulator transition in vanadium dioxide by modifying orbital occupancy," *Nat. Phys.*, vol. 9, pp. 661–666, 2013.

[4] A. Cavalleri, T. Dekorsy, H. H. Chong, J. C. Kieffer, and R. W. Schoenlein, "Evidence for a structurally-driven insulator-to-metal transition in VO 2: A view from the ultrafast timescale [2]," *Phys. Rev. B - Condens. Matter Mater. Phys.*, vol. 70, no. 16, pp. 1–4, 2004.

[5] D. K. Schroder, *Semiconductor material and device characterization.* New York: John Wiley & Sons, 2006.

[6] L. J. Van der Pauw, "A method of measuring specific resistivity and hall effect of discs of arbitray shape," *Philips Res. Rep.*, vol. 13, no. 5, pp. 1–9, 1958.

[7] American Society for Testing and Materials, *Standard Test Methods for Measuring Resistivity and Hall Coefficient and Determining Hall Mobility in Single-Crystal Semiconductors*, vol. 86. West Conshohocken: ASTM International, 2008.

[8] H. van Daal, “Mobility of charge carriers in silicon carbide,” *Phillips Res. reports*, no. Suppl. 3, pp. 1–92, 1965.

[9] T. Yamin, Y. M. Strelniker, and A. Sharoni, “High resolution Hall measurements across the VO 2 metal-insulator transition reveal impact of spatial phase separation,” *Sci. Rep.*, vol. 6, p. 19496, may 2016.

[10] D. Ruzmetov, D. Heiman, B. B. Claflin, V. Narayanamurti, and S. Ramanathan, “Hall carrier density and magnetoresistance measurements in thin-film vanadium dioxide across the metal-insulator transition,” *Phys. Rev. B - Condens. Matter Mater. Phys.*, vol. 79, no. 15, pp. 10–13, 2009.

[11] D. W. Koon and C. J. Knickerbocker, “Effects of macroscopic inhomogeneities on resistive and Hall measurements on crosses, cloverleafs, and bars,” *Rev. Sci. Instrum.*, vol. 67, no. 12, pp. 4282–4285, 1996.

[12] R. Chwang, B. J. Smith, and C. R. Crowell, “Contact size effects on the van der Pauw method for resistivity and Hall coefficient measurement,” *Solid State Electron.*, vol. 17, no. 12, pp. 1217–1227, 1974.

[13] J. M. David and M. G. Buehler, “A numerical analysis of various cross sheet resistor test structures,” *Solid. State. Electron.*, vol. 20, no. 6, pp. 539–543, 1977.

[14] J. H. Park, J. M. Coy, T. Serkan Kasirga, C. Huang, Z. Fei, S. Hunter, and D. H. Cobden, “Measurement of a solid-state triple point at the metal-insulator transition in VO 2,” *Nature*, vol. 500, no. 7463, pp. 431–434, 2013.

[15] J. M. Atkin, S. Berweger, E. K. Chavez, M. B. Raschke, J. Cao, W. Fan, and J. Wu, “Strain and temperature dependence of the insulating phases of VO 2 near the metal-insulator transition,” *Phys. Rev. B - Condens. Matter Mater. Phys.*, vol. 85, no. 2, pp. 1–4, 2012.

[16] V. R. Morrison, R. P. Chatelain, K. L. Tiwari, A. Hendaoui, A. Bruhács, M. Chaker, and B. J. Siwick, “A photoinduced metal-like phase of monoclinic VO2 revealed by ultrafast electron diffraction,” *Science (80-.).*, vol. 346, pp. 445 LP – 448, oct 2014.

[17] S. Suga, M. Taniguchi, M. Fujisawa, H. Kanzaki, A. Fujimiori, H. Daimon, Y. Ueda, K. Kosuge, and S. Kachi, "Vacuum-ultraviolet reflectance and photoemission study of the metal-insulator phase transitions in VO2, V6O13, and V2O3," *Phys. Rev. B*, vol. 41, no. 8, pp. 4993–5009, 1990.

[18] F. Gebhard, *The Mott Metal – Insulator Transitions : Models and Methods.* Springer US, 2010.

[19] M. Imada, A. Fujimori, and Y. Tokura, "Metal-insulator transitions," *Rev. Mod. Phys.*, vol. 70, pp. 1039–1263, oct 1998.

[20] W. H. Rosevear and W. Paul, "Hall Effect in VO2 near the Semiconductor-to-Metal Transition," *Phys. Rev. B*, vol. 7, no. 5, pp. 2109–2111, 1972.

[21] D. Ruzmetov, G. Gopalakrishnan, C. Ko, V. Narayanamurti, and S. Ramanathan, "Three-terminal field effect devices utilizing thin film vanadium oxide as the channel layer," *J. Appl. Phys.*, vol. 107, no. 11, 2010.

[22] D. B. McWhan, A. Menth, J. P. Remeika, W. F. Brinkman, and T. M. Rice, "Metal-Insulator Transitions in Pure and Doped V₂O₃," *Phys. Rev. B*, vol. 7, pp. 1920–1931, mar 1973.

[23] J. C. Slater, "Magnetic Effects and the Hartree-Fock Equation," *Phys. Rev.*, vol. 82, no. 4, pp. 538–541, 1951.

[24] J. Trastoy, A. Camjayi, J. del Valle, Y. Kalcheim, J. P. Crocombette, J. E. Villegas, M. Rozenberg, D. Ravelosona, and I. K. Schuller, "The magnetic origin of the metal-insulator transition in V2O3: Mott meets Slater," *arXiv e-prints*, aug 2018.

[25] I. G. Austin and C. E. Turner, "The nature of the metallic state in V2O3 and related oxides," *Philos. Mag.*, vol. 19, no. 161, pp. 939–949, 1969.

[26] H. R. Rasouli, N. Mehmood, O. Çakıroğlu, E. C. Sürmeli, and T. S. Kasırga, "Synthesis of V2O3 Nanoplates," *arXiv e-prints*, jul 2019.

[27] J. Choi, B. J. Kim, G. Seo, H. T. Kim, S. Cho, and Y. W. Lee, "Magnetic field-dependent ordinary Hall effect and thermopower of VO 2 thin films," *Curr. Appl. Phys.*, vol. 16, no. 3, pp. 335–339, 2016.

[28] C. C. Y. Kwan, C. H. Griffiths, and H. K. Eastwood, "Transport and structural properties of VO2 films," *Appl. Phys. Lett.*, vol. 20, no. 2, pp. 93–95, 1972.

[29] S. Kittiwatanakul, J. Lu, and S. A. Wolf, "Transport anisotropy of epitaxial VO2 films near the metal-semiconductor transition," *Appl. Phys. Express*, vol. 4, no. 9, pp. 2–5, 2011.

[30] J. Wei, Z. Wang, W. Chen, and D. H. Cobden, "New aspects of the metal–insulator transition in single-domain vanadium dioxide nanobeams," *Nat. Nanotechnol.*, vol. 4, pp. 420–424, jul 2009.

[31] J. Wu, Q. Gu, B. S. Guiton, N. P. De Leon, L. Ouyang, and H. Park, "Strain-induced self organization of metal-insulator domains in single-crystalline VO 2 nanobeams," *Nano Lett.*, vol. 6, no. 10, pp. 2313–2317, 2006.

[32] M. M. Fadlelmula, E. C. Sürmeli, M. Ramezani, and T. S. Kasırga, "Effects of Thickness on the Metal-Insulator Transition in Free-Standing Vanadium Dioxide Nanocrystals," *Nano Lett.*, vol. 17, pp. 1762–1767, mar 2017.

[33] K. Yavuz, *Crystal growth and investigations on the effects of hydrogen doping of VO2*. PhD thesis, Bilkent University, mar 2019.

[34] E. Strelcov, A. V. Davydov, U. Lanke, C. Watts, and A. Kolmakov, "In situ monitoring of the growth, intermediate phase transformations and templating of single crystal VO2 nanowires and nanoplatelets," *ACS Nano*, vol. 5, no. 4, pp. 3373–3384, 2011.

[35] H. R. Rasouli, N. Mehmood, O. Cakiroglu, and T. S. Kasirga, "Real time optical observation and control of atomically thin transition metal dichalcogenide synthesis," *Nanoscale*, vol. 11, no. 15, pp. 7317–7323, 2019.

[36] J. F. Ziegler, M. D. Ziegler, and J. P. Biersack, "SRIM - The stopping and range of ions in matter (2010)," *Nucl. Instruments Methods Phys. Res. Sect.*

B Beam Interact. with Mater. Atoms, vol. 268, no. 11-12, pp. 1818–1823, 2010.

[37] J. Wu, Q. Gu, B. S. Guiton, N. P. de Leon, L. Ouyang, and H. Park, "Strain-Induced Self Organization of Metal-Insulator Domains in Single-Crystalline VO 2 Nanobeams," *Nano Lett.*, vol. 6, pp. 2313–2317, oct 2006.

[38] S. Dai, J. Zhang, Q. Ma, S. Kittiwatanakul, A. McLeod, X. Chen, S. G. Corder, K. Watanabe, T. Taniguchi, J. Lu, Q. Dai, P. Jarillo-Herrero, M. Liu, and D. N. Basov, "Phase-Change Hyperbolic Heterostructures for Nanopolaritonics: A Case Study of hBN/VO 2," *Adv. Mater.*, vol. 31, no. 18, pp. 1–6, 2019.

Appendix A

Copyright Permissions

1. Figure 1.5: Reprinted figure with permission from [Morrison et al. (2014). A photoinduced metal-like phase of monoclinic VO2 revealed by ultrafast electron diffraction. Science, 80(346), 445-448.] Copyright (2019) by the American Association for the Advancement of Science.

2. Figure 1.6: Reprinted figure with permission from [Shin et al. Vacuum-ultraviolet reflectance and photoemission study of the metal-insulator phase transitions in VO2, V6O13, and V2O3. Physical Review B 41.8 (1990): 4993.] Copyright (2019) by the American Physical Society.

3. Figure 1.7: Reprinted figure with permission from [Ruzmetov et al. (2009). Hall carrier density and magnetoresistance measurements in thin-film vanadium dioxide across the metal-insulator transition. Physical Review B - Condensed Matter and Materials Physics, 79(15), 10–13.] Copyright (2019) by the American Physical Society. Reprinted with permission from [Yamin et al. (2016). High resolution Hall measurements across the VO2 metal-insulator transition reveal impact of spatial phase separation. Scientific Reports, 6(1), 19496.] Creative Commons Attribution 4.0 License.

4. Figure 1.9: Reprinted figure with permission from [Austin et al. (1969). The nature of metallic state in V2O3 and related oxides. Philosophical Magazine, 19(161), 939-949.] Copyright (2019) by Taylor & Francis.

5. Figure 3.4 and 3.5: Reprinted figure with permission from [Fadlelmula et al. (2017). Effects of Thickness on the Metal-Insulator Transition in Free-Standing Vanadium Dioxide Nanocrystals. Nano Letters, 17, 1762-1767.] Copyright (2019) by the American Chemical Society.